A consistent treatment of dynamic contact angles in the sharp-interface framework with the generalized Navier boundary condition

Tomas Fullana[1,2], Yash Kulkarni[1], Mathis Fricke[3], Stéphane Popinet[1], Shahriar Afkhami[4], Dieter Bothe[3], and Stéphane Zaleski[1,5]

[1]Sorbonne Université and CNRS, Institut Jean Le Rond d'Alembert UMR 7190, F-75005 Paris, France

[2]Laboratory of Fluid Mechanics and Instabilities, School of Engineering, Ecole Polytechnique Fédérale de Lausanne, Lausanne, 1015, Switzerland

[3]Department of Mathematics, TU Darmstadt, Schlossgartenstraße 7, 64289 Darmstadt, Germany

[4]Department of Mathematical Sciences, New Jersey Institute of Technology, Newark, NJ, USA 07102

[5]Institut Universitaire de France, Paris, France

(Received xx; revised xx; accepted xx)

In this work, we revisit the Generalized Navier Boundary condition (GNBC) introduced by Qian et al. in the sharp interface Volume-of-Fluid context. We approximate the singular uncompensated Young stress by a smooth function with a characteristic width ε. We show that the resulting model is consistent with the fundamental kinematics of the contact angle transport described by Fricke, Köhne and Bothe. We implement the model in the geometrical Volume-of-Fluid solver Basilisk using a "free angle" methodology. This means that the dynamic contact angle is not prescribed but reconstructed from the interface geometry and subsequently applied as an input parameter to compute the uncompensated Young stress. We couple this approach to the two-phase Navier Stokes solver and study the withdrawing tape problem with a receding contact line. It is shown that the model is grid-independent and leads to a full regularization of the singularity at the moving contact line. In particular, it is shown that the curvature at the moving contact line is finite and mesh converging. As predicted by the fundamental kinematics, the parallel shear stress component vanishes at the moving contact line for quasi-stationary states (i.e. for $\dot{\theta}_\mathrm{d} = 0$) and the dynamic contact angle is determined by a balance between the uncompensated Young stress and an effective contact line friction. Away from the moving contact line, we confirm that the viscous bending of the interface is well-described by the asymptotic theory of Cox. A non-linear generalization of the original GNBC is proposed, which is closely related to the Molecular Kinetic Theory of wetting.

Key words: dynamic contact line, Volume-of-Fluid method, Generalized Navier Boundary Condition, withdrawing plate, forced dewetting

1. Introduction

The phenomenon of dynamic wetting / dewetting requires a relative motion of the contact line, i.e. the triple line at which the liquid-fluid interface and the solid support's surface meet, against the solid wall. This fundamental process can be modeled in various different ways. If the fluid-interface and the contact line are modeled as a material surface and a material line, respectively, it is clear that the classical no-slip condition is incompatible with the dynamic wetting process. Mathematically, it has been shown that, for a material interface and contact line, the no-slip boundary condition leads to a discontinuity in the velocity as the contact line is approached. Because of that, a viscous fluid develops a non-integrable singularity at the moving contact line. This has been first shown in the seminal paper by Huh & Scriven (1971). Since then, various mathematical models have been developed to resolve the paradox in the continuum mechanical description. In the framework of diffuse interface models, where both the fluid interface and contact line have a finite width characterized by a smooth but rapidly varying order parameter, a motion of the contact line can be achieved by pure diffusion of the order parameter; see Jacqmin (2000). In this case, the motion is driven by gradients of the chemical potential and the contact line is not a material line with respect to the fluid particles. The Interface Formation Model due to Shikhmurzaev (1993, 2008) describes the dynamic wetting process using mass transfer between the bulk phases of the liquid and the interfaces between fluid and solid and fluid gas. Hence, in this case, the contact line can move without hydrodynamic slip as the primary mechanism.

A commonly used approach in the sharp interface framework is to model the interface and the contact line as material objects and to allow for slip between the bulk velocity and the solid wall. The Navier slip condition states that the amount of tangential slip is determined by a balance between the tangential component of the viscous stress (described by the viscous stress tensor $\mathbf{S}$) and a sliding friction force between fluid particles and the solid surface according to

$$-\beta(\mathbf{v}_{\parallel} - \mathbf{U}_w) = (\mathbf{S}\mathbf{n}_{\partial\Omega})_{\parallel}. \tag{1.1}$$

This boundary condition introduces the slip length $L := \eta/\beta$ as the key parameter. Here η denotes the viscosity of the liquid and $\beta > 0$ is a coefficient describing the (sliding) friction between the liquid molecules and the solid surface. Within the Navier slip model, the slip length can be interpreted geometrically as the distance below the solid surface where the linearly extrapolated tangential velocity vanishes. In particular, this implies that, formally, the slip length goes to infinity if the shear stress goes to zero. Indications of a vanishing shear stress in the vicinity of the contact line have been observed in molecular dynamics (MD) simulations by Thompson & Robbins (1989) and others. This phenomenon is commonly referred to as apparent "perfect slip" at the contact line. So, within the model (1.1), the friction parameter β would vanish as the contact line is approached. Besides the mobility of the contact line, the wettability of the solid surface is another key parameter for the physical system. It is usually characterized by the equilibrium contact angle θ_e that the free surface forms with the solid boundary in equilibrium. It can be computed from the surface tension of the liquid-gas, liquid-solid and solid-gas interfaces, using the equation introduced by Young (1805), viz.

$$\sigma \cos\theta_e + \sigma_{ls} - \sigma_{sg} = 0. \tag{1.2}$$

While the latter equation can be easily deduced from variational principles, the dynamics of the contact angle is a much more complex problem and a large variety of empirical models exist. Notably, there is one fundamental relation for the dynamics of the microscopic contact

angle θ_d in the limit of slow velocities of the contact line, which is shared by many of these models:

$$-\zeta U_{cl} = \sigma(\cos\theta_d - \cos\theta_e). \tag{1.3}$$

Here U_{cl} denotes the normal speed of the contact line relative to the solid surface (positive for advancing and negative for a receding contact line) and ζ is the so-called "contact line friction" parameter. Equation (1.3) arises, for example, from the molecular kinetic theory of wetting in the limit of small capillary numbers, i.e. for a slow motion of the contact line (see Blake & Haynes (1969); Blake *et al.* (2015)).

Recently, Fricke *et al.* (2019, 2018) studied the kinematics of the contact angle transport and showed that the rate-of-change of the contact angle is fully determined by the directional tangential derivative of the velocity field $\mathbf{v}$ at the contact line, i.e.

$$\dot{\theta}_d = (\partial_\tau \mathbf{v}) \cdot \mathbf{n}_\Sigma. \tag{1.4}$$

Here $\mathbf{n}_\Sigma$ denotes the interface normal vector and τ is a vector tangential to the interface (see Section 2 for more details). Notably, when applied to the full two-phase flow problem (assuming sufficient regularity of the solution), Equation (1.4) implies that $\dot{\theta}_d$ is proportional to the derivative in the direction normal to the wall of the tangential velocity component. In other words, (1.4) predicts that an apparent perfect slip is acting at the moving contact line if the contact angle does not change in time, i.e. if $\dot{\theta}_d = 0$. Qualitatively, this is consistent with what has been observed in MD simulations. However, it is well-known that the singularity at the moving contact line is only partially relaxed by the Navier slip condition. A logarithmic divergence as a function of the distance to the contact line still exists for the curvature and the pressure, as pointed out by Huh & Mason (1977). Indeed, Fricke & Bothe (2020) showed that the local boundary conditions at the moving contact line are incompatible with each other. As a consequence, the solution cannot possess a C^1-regularity for the velocity up to the contact line. To summarize, the contact angle boundary condition formulated in the standard Navier slip model of the moving contact line is in contradiction with the kinematic evolution law (1.4) and a regular (i.e., piecewise C^1) solution does not exist. However, the introduction of the Navier slip transforms the singularity at the moving contact line into an integrable one and allows for physically meaningful solutions. The physical implications of the pressure singularity is debated in the literature. Shikhmurzaev (2006) argues that the pressure should remain finite because otherwise the model of an incompressible fluid would no longer be valid. On the other hand, it has been demonstrated that the Navier slip model is able to describe various wetting experiments in a satisfactory manner.

The "Generalized Navier Boundary Condition" (GNBC) was first described by Qian *et al.* (2003, 2006*a*,*b*) in the context of diffuse interface models. The key idea of the GNBC is to introduce the *uncompensated Young stress* as an additional force density into the balance equation (1.1). So, in this model, the slip velocity relative to the solid surface is a result of a balance between a sliding friction force, the viscous stress and the uncompensated Young stress. In a sharp interface and sharp contact line formulation, the GNBC can be written as

$$-\beta(\mathbf{v}_\parallel - \mathbf{U}_w) = (\mathbf{S}\mathbf{n}_{\partial\Omega})_\parallel + \sigma(\cos\theta_d - \cos\theta_e)\,\mathbf{n}_\Gamma \delta_\Gamma \quad \text{on} \quad \partial\Omega. \tag{1.5}$$

Notably, the contact line delta distribution δ_Γ appears because, in the sharp contact line formulation, the Young stress is concentrated just on a mathematical curve. Hence, Equation (1.5) should mathematically be understood as an equality of distributions. Provided that the left-hand side, i.e. the sliding friction force, is regular, this implies that the viscous stress component $(\mathbf{S}\mathbf{n}_{\partial\Omega})_\parallel$ should also develop a singularity to make the right-hand regular as well.

This singularity is then balancing with the singularity in the Young stress. This delta function GNBC formulation (DF-GNBC) is applicable in weak formulations of the two-phase flow problem where the contact line delta distribution will translate into an integral over the contact line in the weak formulation (see, e.g, Gerbeau & Lelièvre (2009)). On the other hand, there is no singularity in the Phase Field formulation of the GNBC (PF-GNBC) due to Qian et al., because the thickness of the interface and the contact line is a finite, physical model parameter in this case. Yamamoto *et al.* (2013, 2014) implemented the GNBC approach into a front-tracking-method and studied the dynamics of capillary rise in a tube. In this method, the contact line is transported by an advection of the Lagrangian marker points without a prescribed contact angle. Then the dynamic contact angle is evaluated and used to compute the uncompensated Young stress, which determines the slip velocity profile. Yamamoto et al. noticed that the viscous stress becomes negligible as the contact line is approached. Motivated by this observation, they dropped the viscous stress contribution in (1.5) leading to a "simplified GNBC".

$$-\beta(\mathbf{v}_{\|} - \mathbf{U}_w) = \sigma(\cos\theta_\mathrm{d} - \cos\theta_\mathrm{e})\,\mathbf{n}_\Gamma\delta_\Gamma \quad \text{near} \quad \Gamma. \tag{1.6}$$

It is evident that, by taking the inner product with the contact line normal vector, Eq. (1.6) can be reduced to an equation equivalent to (1.3) if the delta distribution is approximated with a regular function over a finite width.

Yamamoto *et al.* (2013, 2014) smoothed the delta distribution over a region of approximately four grid points. Using this estimate as the characteristic width of the delta function, the authors concluded that

$$U_\mathrm{cl} \approx \frac{L}{\Delta}\frac{\sigma(\cos\theta_\mathrm{e} - \cos\theta_\mathrm{d})}{\eta}, \tag{1.7}$$

where Δ is the grid size. Obviously, the contact line speed in (1.7) can only be grid-independent if also the slip length is chosen in proportion to the grid size, i.e. if $L \sim \Delta$. Consequently, they fixed the parameter $\chi := L/\Delta$ in their simulations. The approach was extended by using the Cox-Voinov relation for θ_d in Yamamoto *et al.* (2014). Later, Yamamoto *et al.* (2016) used this method to study the withdrawing plate problem with a single wettable defect. Recently, the GNBC front-tracking approach was extended by Kawakami *et al.* (2023) using a so-called "rolling belt-model" inspired by the work of Lukyanov & Pryer (2017). Chen *et al.* (2019) used the GNBC in a Front Tracking method to study the coalescence-induced self-propelled motion of droplets on a solid surface. Shang *et al.* (2018) used a quite similar method to study droplet spreading and the motion of drops on surfaces subject to a shear flow. All these methods have in common that the uncompensated Young stress is distributed over a characteristic distance, which is related to the mesh size.

In the present work, we aim at a regularization of the Young stress in a sharp interface setting. This is achieved by approximating the Young stress by a smooth function with a characteristic width ε which is chosen *independently* of the computational mesh but treated as a model parameter. We shall call this model the "smooth-function GNBC" (SF-GNBC) in the following. It has been shown recently by Kulkarni *et al.* (2023) that this model admits a local C^2-regularity of the velocity in the vicinity of the moving contact line. In the present paper, we develop a novel implementation of the SF-GNBC in a geometrical Volume-of-Fluid method. This method should be consistent with the fundamental kinematic law (1.4). Therefore, the dynamic contact angle is not prescribed but is reconstructed from the volume fraction field in a neighborhood of the contact line. As one important preliminary

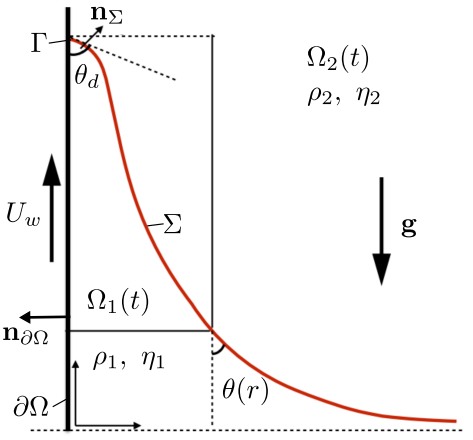

Figure 1: Mathematical notation for the withdrawing tape setup.

step, we validate this "free contact angle" methodology by studying the advection problem by a *prescribed* velocity field (see Fricke *et al.* (2020)). In this case, the interface and the contact line are transported without a boundary condition for the contact angle and the results are validated against analytical solutions of (1.4). Moreover, we couple this method to the SF-GNBC model and use the reconstructed contact angle as an input parameter for θ_d to compute the uncompensated Young stress in the simulation.

We study the withdrawing tape problem as a prototypical example for a dynamic dewetting process. The setup follows the previous work by Afkhami *et al.* (2018). The solid wall is moving upwards with velocity $U_w \geqslant 0$ in the laboratory frame (see Figure 1). So we study the case of a receding contact line. We define the (global) capillary number with respect to the wall speed as

$$\mathrm{Ca} := \frac{\eta U_w}{\sigma}.$$

For convenience, we define the *contact line* capillary number using the negative contact line speed, i.e. (note that the contact line speed U_cl is always measured relative to the solid)

$$\mathrm{Ca}_\mathrm{cl} := \frac{\eta(-U_\mathrm{cl})}{\sigma}.$$

In a quasi-stationary state, we have $-U_\mathrm{cl} = U_w$ and hence $\mathrm{Ca} = \mathrm{Ca}_\mathrm{cl}$. With this definition, we can always work with positive values for the capillary number. Notice that, in the literature, one will also find the convention that Ca_cl is negative for a receding contact line and positive for an advancing contact line.

Structure of this article

The mathematical derivation of the GNBC in a sharp-interface framework is revisited in Section 2. It is shown that the GNBC can be obtained as a combined closure relation for the dissipation due to slip along the liquid-solid surface and the contact line dissipation. Using the laws of kinematics, we derive the contact angle evolution equation in Section 2.4 and show that (1.3) holds for quasi-stationary states. The numerical implementation of the method in the geometrical Volume-of-Fluid solver is described in Section 3. We validate the

Table 1: Description of Symbols

Symbol	Description	Units
ρ	Density	kg/m^3
η	Viscosity	Pa·s
σ	Surface Tension	N/m
$\mathbf{v}$	Velocity	m/s
β	Friction Coefficient	Pa·s/m
$\mathbf{g}$	Gravitational Acceleration	m/s^2
$\mathbf{D}$	Rate-of-Deformation Tensor	1/s
$\mathbf{S} = 2\eta\mathbf{D}$	Viscous Stress Tensor	Pa
Σ	Interface	-
V_Σ	Interface Normal Speed	m/s
$\mathbf{n}_\Sigma$	Interface Normal	-
$\kappa = -\nabla_\Sigma \cdot \mathbf{n}_\Sigma$	Interface Mean Curvature	1/m
Γ	Contact Line	-
U_{cl}	Contact Line Speed	m/s
$\mathbf{n}_\Gamma$	Contact Line Normal (tangential to $\partial\Omega$)	-
$\partial\Omega$	Solid Boundary	-
$\mathbf{n}_{\partial\Omega}$	Unit Outer Normal to Ω	-
U_w	Wall Speed	m/s
$\mathbf{U}_w$	Wall Velocity	m/s
$L = \eta/\beta$	Slip Length	m
Ca	Wall Capillary Number	-
$\mathrm{Ca}_{\mathrm{cl}}$	Contact Line Capillary Number	-
$\mathrm{Ca}_{\mathrm{loc}}$	Capillary Number in the lab frame of reference	-
$\mathrm{Ca}_{\mathrm{tr}}$	Transition Capillary Number	-
ζ	Contact Line Friction	Pa·s
θ_{e}	Static Contact Angle	rad
θ_{d}	Dynamic Microscopic Contact Angle	rad
θ_Δ	Numerical contact angle observed at the contact line	rad
θ_{s}	Steady state contact angle	rad

numerical method by studying the kinematic transport of the contact angle and the curvature at the contact line. The results for the withdrawing tape problem are discussed in detail in Section 4. In particular, it is shown that the results are grid-independent. Notably, we can demonstrate by a mesh study that, unlike for the Navier slip model, the curvature at the contact line converges to a finite value. Away from the contact line, we show that the viscous bending of the interface is well-described by the hydrodynamic theory of Cox. Finally, we conclude this study by an outlook to a non-linear variant of the GNBC, which can be derived as a non-linear closure of the entropy production described earlier in Section 2.

2. Mathematical Modeling

2.1. *Governing equations*

We employ the sharp-interface / sharp-contact line continuum modeling approach. We start from the incompressible, two-phase Navier Stokes equations with surface tension for Newtonian fluids under isothermal conditions (see, e.g., Slattery (1999); Prüss & Simonett

(2016)). Inside the fluid phases, the governing equations are

$$\partial_t(\rho\mathbf{v}) + \nabla\cdot(\rho\mathbf{v}\otimes\mathbf{v}) + \nabla p = \nabla\cdot\mathbf{S} + \rho\mathbf{g}, \tag{2.1}$$

$$\nabla\cdot\mathbf{v} = 0 \tag{2.2}$$

with the viscous stress tensor†

$$\mathbf{S} = 2\eta\mathbf{D} = \eta(\nabla\mathbf{v} + \nabla\mathbf{v}^{\mathsf{T}}).$$

These bulk equations are accompanied by jump conditions at the interface $\Sigma(t)$. The interface is modeled as a hypersurface (i.e. it has zero thickness) and separates the domain Ω into two bulk phases $\Omega_{1,2}(t)$ occupied by the two fluid phases (see Fig. 1). Assuming that no phase change occurs in the system, the normal component of the adjacent fluid velocities $\mathbf{v}_{1,2}$ at the interface are coinciding and equal to the speed of normal displacement V_Σ of the interface, resulting in the kinematic boundary condition

$$V_\Sigma = \mathbf{v}\cdot\mathbf{n}_\Sigma \quad \text{on} \quad \Sigma(t), \tag{2.3}$$

where $\mathbf{n}_\Sigma$ is the interface unit normal field. Additionally, no-slip between the fluid phases is usually assumed. Assuming further that the surface tension σ is constant, the jump conditions for mass and momentum read as

$$[\![\mathbf{v}]\!] = 0, \quad [\![p\mathbb{I} - \mathbf{S}]\!]\,\mathbf{n}_\Sigma = \sigma\kappa\mathbf{n}_\Sigma \quad \text{on} \quad \Sigma(t). \tag{2.4}$$

Here $\kappa := -\nabla_\Sigma\cdot\mathbf{n}_\Sigma$ is twice the mean curvature of the interface and

$$[\![\psi]\!](t,\mathbf{x}) := \lim_{h\to 0^+}(\psi(t,\mathbf{x}+h\mathbf{n}_\Sigma) - \psi(t,\mathbf{x}-h\mathbf{n}_\Sigma))$$

is the jump of a quantity ψ across the interface. We assume that the solid boundary $\partial\Omega$ is not able to store mass, i.e. we assume it to be impermeable. We consider an inertial frame of reference where the wall is moving parallel to itself with a velocity $U_w \geqslant 0$ upwards (see Fig. 1). The impermeability condition in this frame of reference reads as

$$\mathbf{v}_\perp = 0 \quad \text{on } \partial\Omega, \tag{2.5}$$

where $\mathbf{v}_\perp = (\mathbf{v}\cdot\mathbf{n}_{\partial\Omega})\,\mathbf{n}_{\partial\Omega}$ denotes the normal part of the velocity with respect to $\partial\Omega$. In order to obtain a closed model, the system of equations (2.1)-(2.5) must be complemented by (one or more) additional boundary conditions describing

(i) the **wettability** of the solid (i.e. the static and dynamic contact angle) and

(ii) the **mobility** of the contact line (i.e. the tangential velocity $\mathbf{v}_\parallel$ at the solid boundary).

These boundary conditions are closure relations for the continuum mechanical description and must be thermodynamically consistent, i.e. they must obey the first and second law of thermodynamics. To arrive at a consistent closure, we consider the available energy functional consisting of the kinetic energy of the bulk phases and the surface energies of the liquid-gas interface as well as the wetted area $W(t) \subset \partial\Omega$, i.e.

$$E(t) := \int_{\Omega\setminus\Sigma(t)} \frac{\rho|\mathbf{v}|^2}{2}\,dV + \int_{\Sigma(t)} \sigma\,dA + \int_{W(t)} \sigma_w\,dA.$$

Here $\sigma = \sigma_{\mathrm{lg}} > 0$ denotes the surface tension coefficient of the liquid-gas interface and

$$\sigma_{\mathrm{w}} = \sigma_{\mathrm{ls}} - \sigma_{\mathrm{sg}}$$

† We use the symbol $\mathbf{D} = \frac{1}{2}(\nabla\mathbf{v} + \nabla\mathbf{v}^{\mathsf{T}})$ for the rate-of-deformation tensor.

is the specific energy density for wetting the solid surface. Note that σ_w might be negative, as we see from Young's equation

$$\sigma \cos\theta_e + \sigma_w = 0, \tag{2.6}$$

which defines the "static" or "equilibrium" contact angle θ_e. It is a purely mathematical exercise (see Fricke (2021) (Appendix A) for details) to compute the rate of change $\dot{E}$ for a sufficiently regular solution of (2.1)-(2.5) (in the absence of external forces, i.e. for $\mathbf{g} = 0$). The result reads as

$$\frac{dE}{dt} = -2\int_{\Omega\setminus\Sigma(t)} \eta \mathbf{D} : \mathbf{D}\, dV + \int_{\partial\Omega} (\mathbf{v}_\parallel - \mathbf{U}_w) \cdot (\mathbf{S}\mathbf{n}_{\partial\Omega})_\parallel \, dA + \int_{\Gamma(t)} \sigma(\cos\theta_d - \cos\theta_e)\, U_{cl}\, dl. \tag{2.7}$$

In this formulation with a continuous velocity field, the scalar contact line speed (measured relative to the solid) is given as

$$U_{cl} = \mathbf{v} \cdot \mathbf{n}_\Gamma - U_w.$$

Closure relations are required to satisfy the second law of thermodynamics† $\dot{E} \leqslant 0$. A linear closure for the second integral in (2.7) yields the well-known Navier slip condition, i.e.

$$-\beta(\mathbf{v}_\parallel - \mathbf{U}_w) = (\mathbf{S}\mathbf{n}_{\partial\Omega})_\parallel \quad \text{with a friction coefficient} \quad \beta \geqslant 0. \tag{2.8}$$

Using the slip lenth parameter $L = \eta/\beta$, one may reformulate (2.8) as

$$\mathbf{v}_\parallel + 2L(\mathbf{D}\mathbf{n}_{\partial\Omega})_\parallel = \mathbf{U}_w. \tag{2.9}$$

The third integral in (2.7) suggests that the dynamic contact angle θ_d, which is *mathematically* defined as the angle of intersection‡ of the free surface Σ with the solid boundary $\partial\Omega$, i.e.

$$\cos\theta_d := -\mathbf{n}_\Sigma \cdot \mathbf{n}_{\partial\Omega} \quad \text{at } \Gamma(t),$$

should be linked to the contact line speed U_{cl}. A linear closure leads to the well-known condition

$$-\zeta U_{cl} = \sigma(\cos\theta_d - \cos\theta_e) \quad \text{with a (contact line) friction coefficient} \quad \zeta \geqslant 0. \tag{2.10}$$

Note that also more general contact angle boundary conditions are possible if a non-linear closure relation is employed. To summarize, the "standard model"¶ based on the Navier slip condition is given by Equations (2.1)-(2.5), (2.9) together with (2.10) or a non-linear variant of the form

$$\theta_d = f(U_{cl}) \quad \text{on} \quad \Gamma(t). \tag{2.11}$$

To ensure thermodynamic consistency, we require that

$$\eta \geqslant 0,\ \sigma \geqslant 0,\ L \geqslant 0,\ U_{cl}(f(U_{cl}) - \theta_e) \geqslant 0.$$

As shown by Fricke & Bothe (2020), there is an inconsistency of boundary conditions in the standard model because the evolution of the contact angle is determined by the contact

† Note that we assume an isothermal system here. In this case, we may directly consider the change in available energy.

‡ Note that, in order to define the contact angle θ_d, we have to assume that interface $\Sigma(t)$ has a well-defined normal field up to the boundary. This is usually the case even if the mean curvature of $\Sigma(t)$ is singular at the contact line.

¶ The mathematical model (2.1)-(2.5), (2.9), (2.10) is one of the most commonly applied models for dynamic wetting in the literature. However, there are many more modeling approaches which aim at a regularization of the singularity and a prediction of the dynamics of wetting. For a survey of the field, we refer to the references de Gennes *et al.* (2004); Blake (2006); Shikhmurzaev (2008); Bonn *et al.* (2009); Snoeijer & Andreotti (2013); Marengo & De Coninck (2022)

angle boundary condition (say (2.10)) *as well as* by the flow in the vicinity of the contact line according to (1.4). As a consequence, a regular solution of the system does not exist but a weak singularity is present at the contact line as shown already in Huh & Mason (1977).

2.2. *Formal derivation of the GNBC*

It is important to note that the GNBC was originally formulated in a *diffuse* interface framework (see Qian *et al.* (2003, 2006*a*)). However, the GNBC can be formally understood in the sharp interface model as a *combined closure* for the terms in the entropy production (2.7) which arise from the contact line motion and from slip at the solid-liquid boundary. For this purpose, we consider the sum of the wall and the contact line dissipation, given as

$$\mathcal{T} = \int_{\partial\Omega} (\mathbf{v}_\parallel - \mathbf{U}_w) \cdot (\mathbf{S}\mathbf{n}_{\partial\Omega})_\parallel \, dA + \sigma \int_{\Gamma(t)} (\cos\theta_\mathrm{d} - \cos\theta_\mathrm{e}) \, U_\mathrm{cl} \, dl.$$

By introducing the contact line delta distribution δ_Γ, one can rewrite $\mathcal{T}$ as a single integral over the entire solid boundary $\partial\Omega$ according to

$$\mathcal{T} = \int_{\partial\Omega} \left((\mathbf{S}\mathbf{n}_{\partial\Omega})_\parallel + \sigma(\cos\theta_\mathrm{d} - \cos\theta_\mathrm{e}) \, \mathbf{n}_\Gamma \delta_\Gamma \right) \cdot (\mathbf{v}_\parallel - \mathbf{U}_w) \, dA.$$

So, formally, a linear closure relation is provided by the generalized Navier boundary condition

$$-\beta(\mathbf{v}_\parallel - \mathbf{U}_w) = (\mathbf{S}\mathbf{n}_{\partial\Omega})_\parallel + \sigma(\cos\theta_\mathrm{d} - \cos\theta_\mathrm{e}) \, \mathbf{n}_\Gamma \delta_\Gamma \quad \text{on} \quad \partial\Omega \tag{2.12}$$

with a friction coefficient $\beta > 0$. Notice that the "delta function GNBC" (DF-GNBC) should be understood in the sense of distributions.

2.3. *Approximation of the delta distribution over a finite region*

A possible approach for regularization is to approximate the contact line delta distribution in (2.12) by a smooth function over a finite transition region with characteristic width ε. Note that this approach also requires to extend the definition of the contact angle θ_d and the contact line normal $\mathbf{n}_\Gamma$ away from the sharp contact line. Then, the deviation of the contact angle from the equilibrium value appears in the velocity boundary condition leading to a balance between sliding friction forces due to slip along the solid boundary, the tangential component of the viscous stress at the boundary and the uncompensated Young force. If extensions of θ_d and $\mathbf{n}_\Gamma$ on a local neighborhood of the contact line are available, one may approximate (2.12) by

$$-(\mathbf{v}_\parallel - \mathbf{U}_w) = 2L(\mathbf{D}\mathbf{n}_{\partial\Omega})_\parallel + \frac{\sigma}{\beta}[(\cos\theta_\mathrm{d} - \cos\theta_\mathrm{e}) \, \mathbf{n}_\Gamma \hat{\delta}_\Gamma], \tag{2.13}$$

where $\hat{\delta}_\Gamma$ is a smooth approximation of δ_Γ. Notably, the dynamic contact angle is not prescribed explicitly in this approach. Instead, the dynamics of the contact angle is determined by (2.13) and the kinematics of the interface transport.

2.4. *Kinematics of the dynamic contact angle*

We derive the evolution law for the contact angle, given a sufficiently regular solution of the SF-GNBC model (2.1)-(2.5) and (2.13). Below, we consider the limit of the free surface case, where one phase is assumed to be a dynamically passive gas at a constant pressure. The GNBC condition, evaluated at the contact line, reads as

$$\beta(\mathbf{v}_\parallel - \mathbf{U}_w) + (\mathbf{S}\mathbf{n}_{\partial\Omega})_\parallel + \frac{1}{\varepsilon}\sigma(\cos\theta_\mathrm{d} - \cos\theta_\mathrm{e}) \, \mathbf{n}_\Gamma = 0 \quad \text{at} \quad \Gamma, \tag{2.14}$$

where $\varepsilon > 0$ is a small parameter describing the characteristic length over which $\hat{\delta}_\Gamma$ is non-zero. By taking the inner product with the contact line normal vector, we obtain the relation

$$\frac{U_{\mathrm{cl}}}{L} + \langle \mathbf{n}_\Gamma, (\nabla \mathbf{v})\, \mathbf{n}_{\partial\Omega} \rangle + \langle (\nabla \mathbf{v})\, \mathbf{n}_\Gamma, \mathbf{n}_{\partial\Omega} \rangle + \frac{\sigma}{\varepsilon \eta} (\cos\theta_{\mathrm{d}} - \cos\theta_{\mathrm{e}}) = 0 \quad \text{at } \Gamma. \tag{2.15}$$

Using the kinematic evolution equation for the contact angle derived in Fricke *et al.* (2019), one can show that the rate-of-change of the contact angle $\dot{\theta}_{\mathrm{d}}$ is given by

$$2\dot{\theta}_{\mathrm{d}} = -\langle \mathbf{n}_\Gamma, (\nabla \mathbf{v})\, \mathbf{n}_{\partial\Omega} \rangle\,. \tag{2.16}$$

Moreover, it follows from the impermeability condition that the term $\langle \nabla \mathbf{v}\, \mathbf{n}_\Gamma, \mathbf{n}_{\partial\Omega} \rangle$ vanishes for a flat solid boundary. Therefore, we obtain the contact angle evolution law for a regular solution of the SF-GNBC model. In this case, it reads as

$$\boxed{\dot{\theta}_{\mathrm{d}} = \frac{U_{\mathrm{cl}}}{2L} + \frac{1}{\varepsilon}\frac{\sigma}{2\eta}(\cos\theta_{\mathrm{d}} - \cos\theta_{\mathrm{e}}).} \tag{2.17}$$

2.5. *Remarks*

(i) Compared to the standard Navier slip model (see Fricke *et al.* (2019) for details), the uncompensated Young stress leads to an additional term in the equation for $\dot{\theta}_{\mathrm{d}}$, which reads as

$$\frac{1}{\varepsilon}\frac{\sigma}{2\eta}(\cos\theta_{\mathrm{d}} - \cos\theta_{\mathrm{e}}).$$

Obviously, the latter term is negative for $\theta_{\mathrm{d}} > \theta_{\mathrm{e}}$ (and positive for $\theta_{\mathrm{d}} < \theta_{\mathrm{e}}$) and, hence, drives the system towards equilibrium.

(ii) An important consequence of the GNBC for *quasi-stationary* states is that it defines a functional dependence between the dynamic contact angle and contact line speed. In fact, setting $\dot{\theta}_{\mathrm{d}} = 0$ leads to the relation

$$\mathrm{Ca}_{\mathrm{cl}} = \frac{\eta(-U_{\mathrm{cl}})}{\sigma} = \frac{L}{\varepsilon}\,(\cos\theta_{\mathrm{d}} - \cos\theta_{\mathrm{e}}), \tag{2.18}$$

or, equivalently, to

$$-(\beta\varepsilon)\, U_{\mathrm{cl}} = \sigma(\cos\theta_{\mathrm{d}} - \cos\theta_{\mathrm{e}}). \tag{2.19}$$

By comparing (2.19) with (2.10), we see that the contact line friction parameter can be indentified with the product of the "bulk friction" in the Navier slip condition and the width of the contact line region, i.e.

$$\zeta = \beta\varepsilon. \tag{2.20}$$

The latter equation has been proposed before by Blake *et al.* (2015) in the context of the molecular kinetic theory. Physically, it indicates that, within the present modeling framework, there is only *one* friction mechanism that affects both the slip at the solid boundary and the dynamics of the microscopic contact angle.

(iii) From (2.16) we conclude that the stress component $\langle \mathbf{n}_\Gamma, (\nabla \mathbf{v})\, \mathbf{n}_{\partial\Omega} \rangle$ vanishes at the contact line for quasi-stationary states, i.e. for $\dot{\theta} = 0$. So, there appears to be "perfect slip" at the contact line in that case. Actually, the concepts of the "apparent slip length" L_a (see Fig. 2) and the physical slip parameter defined as $L = \eta/\beta$ must be distinguished for the GNBC model. In fact, the uncompensated Young stress is able to reverse the sign of the velocity gradient at the contact line. In this case, fluid particles at the solid boundary may have a larger tangential velocity than the fluid particles slightly above the boundary. This

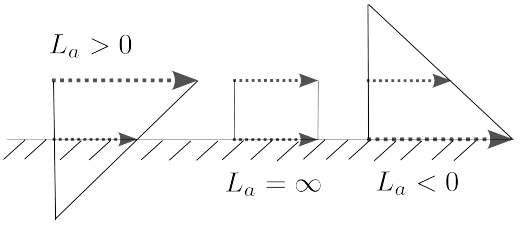

Figure 2: Different cases for the apparent slip length L_a: positive, perfect and negative slip (reference frame with $U_w = 0$).

situation corresponds to a *negative* apparent slip length (see Fig. 2). It is, however, caused by the uncompensated Young stress in the velocity boundary condition. The physical slip length parameter L is still positive and finite in all cases.

(iv) Note that (2.17) can be phrased as a generalized mobility law of the form

$$U_{\mathrm{cl}} = f(\theta_{\mathrm{d}}, \dot{\theta}_{\mathrm{d}}).$$

Therefore, the contact line speed depends on the contact angle θ_{d} but also on its rate-of-change $\dot{\theta}_{\mathrm{d}}$ which, in turn, can be computed from $\nabla \mathbf{v}$ (see Fricke *et al.* (2019)). In this sense, the contact line speed in the GNBC model depends on the flow in the vicinity of the contact line. Such a kind of non-local dependence has been discussed in the literature in the context of the so-called "hydrodynamic assist" (see, e.g, Blake *et al.* (1994, 2015)).

(v) Moreover, the GNBC can be understood as an *inhomogeneous* Robin condition for the velocity. Hence, the GNBC enforces a flow whenever $\theta_{\mathrm{d}} \neq \theta_{\mathrm{e}}$. In contrast to the standard model, the GNBC model is able to describe the relaxation process of the contact angle.

3. Numerical Methods

3.1. *The Volume-Of-Fluid method*

The Volume-Of-Fluid (VOF) method for representing fluid interfaces coupled with a flow solver is well-known to be suited for solving interfacial flows (see e.g. Scardovelli & Zaleski (1999); Popinet & Zaleski (1999); Tryggvason *et al.* (2011); Marić *et al.* (2020)). We use the free software *Basilisk*, a platform for the solution of partial differential equations on adaptive Cartesian meshes (Popinet (2009, 2015, 2018)). For a two-phase flow, the volume fraction $c(\mathbf{x}, t)$ is defined as the integral of the first fluid's characteristic function in the control volume. The volume fraction $c(\mathbf{x}, t)$ is used to define the density and viscosity in the control volume according to

$$\begin{aligned} \rho(c) &\equiv c\rho_1 + (1-c)\rho_2, \\ \mu(c) &\equiv c\mu_1 + (1-c)\mu_2, \end{aligned} \tag{3.1}$$

with ρ_1, ρ_2 and μ_1, μ_2 the densities and viscosities of the phase 1 and 2 respectively.
The advection equation for the density is then replaced by the equation for the volume fraction

$$\partial_t c + \nabla \cdot (c\mathbf{v}) = 0 \tag{3.2}$$

The projection method is used to solve the incompressible Navier-Stokes equations combined with a Bell-Collela-Glaz advection scheme and a VOF method for interface tracking. The resolution of the surface tension term is directly dependent on the accuracy of the curvature calculation. The Height-Function methodology, described in Afkhami & Bussmann (2008, 2009), is a VOF-based technique for calculating interface normals and curvatures. About each interface cell, fluid 'heights' are calculated by summing fluid volume in the grid direction

closest to the normal of the interface. In two dimensions, a 7×3 stencil around an interface cell is constructed and the heights are evaluated by summing volume fractions horizontally

$$h_j = \sum_{k=i-3}^{k=i+3} c_{j,k}\, \Delta, \tag{3.3}$$

with $c_{j,k}$ the volume fraction and Δ the grid spacing. The heights are then used to compute the interface normal $\mathbf{n}_\Sigma$ and the curvature κ

$$\begin{aligned} \mathbf{n}_\Sigma &= (h_x, -1), \\ \kappa &= \frac{h_{xx}}{\left(1 + h_x^2\right)^{3/2}}, \end{aligned} \tag{3.4}$$

where h_x and h_{xx} are discretized using second-order central differences. The orientation of the interface, characterized by the contact angle – the angle between the normal to the interface at the contact line and the normal to the solid boundary – is imposed in the contact line cell. It is important to note that a numerical specification of the contact angle affects the overall flow calculation in two ways:

(i) it defines the orientation of the interface reconstruction in cells that contain the contact line;

(ii) it influences the calculation of the surface tension term by affecting the curvature computed in cells at and near the contact line.

We now present the numerical implementation of the Generalized Navier Boundary Condition as written in (2.14). The boundary condition is applied on the solid surface with a smoothing function that takes into account the relative position along the boundary with respect to the contact line

$$\beta(\mathbf{v}_\parallel - \mathbf{U}_w) + (\mathbf{S}\mathbf{n}_{\partial\Omega})_\parallel + \mathrm{f}(\frac{x}{\varepsilon})\, \sigma(\cos\theta_\mathrm{d} - \cos\theta_\mathrm{e})\, \mathbf{n}_\Gamma = 0 \quad \text{on} \quad \partial\Omega, \tag{3.5}$$

with $\mathrm{f}\left(\frac{x}{\varepsilon}\right)$ the discrete dirac function defined as

$$\mathrm{f}\left(\frac{x}{\varepsilon}\right) = \frac{\left(1 - \tanh^2\left(\frac{x}{\varepsilon}\right)\right)}{\varepsilon}. \tag{3.6}$$

The boundary condition can be expressed as a inhomogeneous Robin boundary condition for the parallel velocity $\mathbf{v}_\parallel$, as outlined below

$$\mathbf{v}_\parallel + \frac{1}{\beta}(\mathbf{S}\mathbf{n}_{\partial\Omega})_\parallel = \mathbf{U}_w + \frac{1}{\beta}\,\mathrm{f}(\frac{x}{\varepsilon})\, \sigma(\cos\theta_\mathrm{e} - \cos\theta_\mathrm{d})\, \mathbf{n}_\Gamma \quad \text{on} \quad \partial\Omega. \tag{3.7}$$

We use the Robin boundary condition (slip) that was implemented in the same framework in Fullana *et al.* (2020) and tested as a localized slip boundary condition in Lācis *et al.* (2020). The difference lies now in the space dependent right-hand-side of (3.7). The uncompensated Young's stress, that only acts at the contact line through the discrete dirac function, needs to be computed at each grid point.

The GNBC approach in this study stands out for its "free angle" method. Instead of setting the dynamic angle θ_d, we reconstruct it from the interface geometry and use it as an input parameter to calculate the right-hand side of (3.7). To impose such a consistent angle we use the derived a relation between the numerical contact angle and an "apparent" angle, a specific distance away from the wall, as shown in Fricke (2021). The numerical angle can be

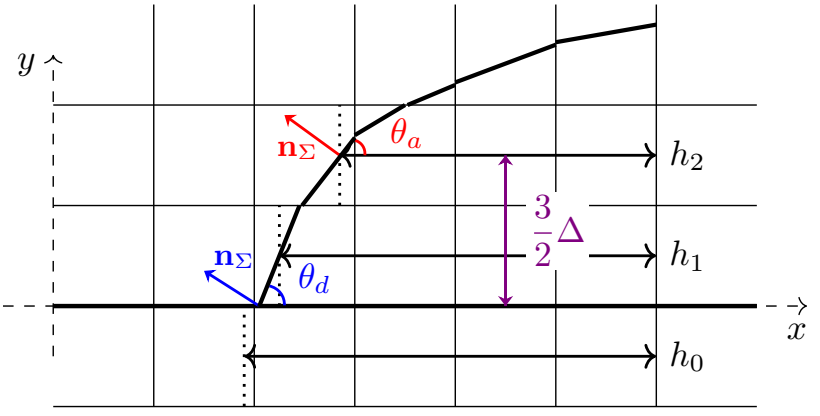

Figure 3: Extrapolation of the contact angle θ_d using the apparent angle θ_a located $3/2\,\Delta$ away from the wall.h_0 to h_2 denote the horizontal heights.

extrapolated using the following formula

$$\theta_d = \theta_a + \frac{3}{2}\Delta\frac{\kappa\sqrt{1+(h_y)^2}}{\sin(\theta_a)}. \tag{3.8}$$

Here, θ_d represents the extrapolated angle, θ_a is the apparent angle, Δ denotes the grid spacing, κ stands for curvature, and h_y represents the first-order derivative of the height function in the y direction (normal to the wall). Figure 3 provides a schematic illustration of this extrapolation process. Once the extrapolated angle is computed, we enforce it through height functions, similar to a regular contact angle. Algorithm 1 is a concise summary of the two-step procedure to apply the "free angle" GNBC in the VOF framework.

Algorithm 1: Two-step "free angle" GNBC pseudo-code

for *each boundary cell* **do**
1. Locate the contact line cell
2. Locate the cell one grid point above the contact line
3. Compute the apparent angle θ_a using the unit normal $\mathbf{n}_\Sigma$
4. Compute the first order derivative of the height function h_x
5. Compute the interface curvature κ
6. Compute the extrapolated angle θ_d using (3.8)

end

7. Apply θ_d at the contact line through height functions

for *each boundary cell* **do**
8. Compute the right-hand-side of (3.7) using θ_d and θ_e

end

9. Apply the boundary condition for $\mathbf{v}_\parallel$ using (3.7)

3.2. *Kinematic transport of the contact angle*

We validate the angle extrapolation methodology presented in (3.8) through an analysis of the kinematic transport of the contact angle in a simplified setup. Leveraging kinematic considerations, Fricke (2021) derived an analytical solution for the transport of the contact

angle and the curvature in the case of an incompressible flow. To validate the present approach within the VOF framework, we conduct simulations of an oscillating disk in contact with the domain boundary. These simulations are carried out for various grid sizes.

The setup involves a disk with a diameter $D = 1$ in a 2×2 domain, initially placed over a static substrate with a contact angle of $\theta_0 = 90^\circ$. The velocity field across the entire domain is defined as:

$$v_x = c_1 \cos(\pi t)x + c_2 \cos(\pi t)y, \tag{3.9}$$

$$v_y = c_1 \cos(\pi t)y, \tag{3.10}$$

Here, v_x and v_y represent the x and y components of the velocity, while c_1 and c_2 are positive constants. We aim to validate the accuracy and reliability of the angle extrapolation methodology under varying grid sizes, where we only consider the advection equation of the color function (3.2).

The prescribed incompressible velocity field (3.9) will induce oscillations of the drop in both vertical and horizontal directions. The angle formed at the contact line will be affected by this motion and vary in time. From the relations derived in Fricke *et al.* (2020), we will compare the observed numerical contact angle with the analytical one θ_{an}, given by the formula

$$\theta_{an} = \frac{\pi}{2} + \tan^{-1}\left(\frac{-1}{\tan\theta_0} e^{2\,c_1\,S} + \frac{c_1}{2\,c_2} e^{2\,c_1\,S} - 1\right), \tag{3.11}$$

with

$$S = \frac{\sin(\pi t)}{\pi}, \tag{3.12}$$

and the numerical curvature with the analytical one κ_{an}, that can be expressed as the solution of an ordinary differential equation

$$\frac{\partial \kappa_{an}}{\partial t} = -3\,\kappa_{an}\,\cos(\pi t)\,(c_1\,\cos^2(\theta_{an}) - c_2\,\cos(\theta_{an})\,\sin(\theta_{an}) - c_1\,\sin^2(\theta_{an})), \tag{3.13}$$

with the initial condition $\kappa_0 = 2/D = 2$. We conduct two sets of simulations to evaluate the method. In the first set, the contact angle remains constant at 90° (corresponding to a default symmetric boundary condition for the color function), while in the second set, we enforce the extrapolated angle. The simulations run until a final time $T = 10$, and we examine the convergence of the method with grid sizes varying from 16 to 128 points per diameter. In Figure 4, we summarize the obtained results. The extracted contact angle shows an increased accuracy and rapid convergence compared to the analytical solution, thanks to the angle extrapolation methodology. Furthermore, the curvature is accurately transported in this scenario, while it diverges in the case where the contact angle is fixed at 90°.

4. Results

We apply the numerical method for the flow-consistent Generalized Navier Boundary Condition (GNBC) to the pulling plate setup, following the approach discussed in Section 1. This setup is akin to the one investigated by Afkhami *et al.* (2018).

Figure 5 displays the results of a steady-state simulation using the present GNBC method. The Figure is presented in the reference frame of the contact line, where the contact line remains stationary while the left wall is pulled upwards. The velocity field relaxes, creating a stagnation point at the contact line. Additionally, the streamlines reveal another stagnation point formed above the interface in the lighter phase. It's worth noting that the characteristics

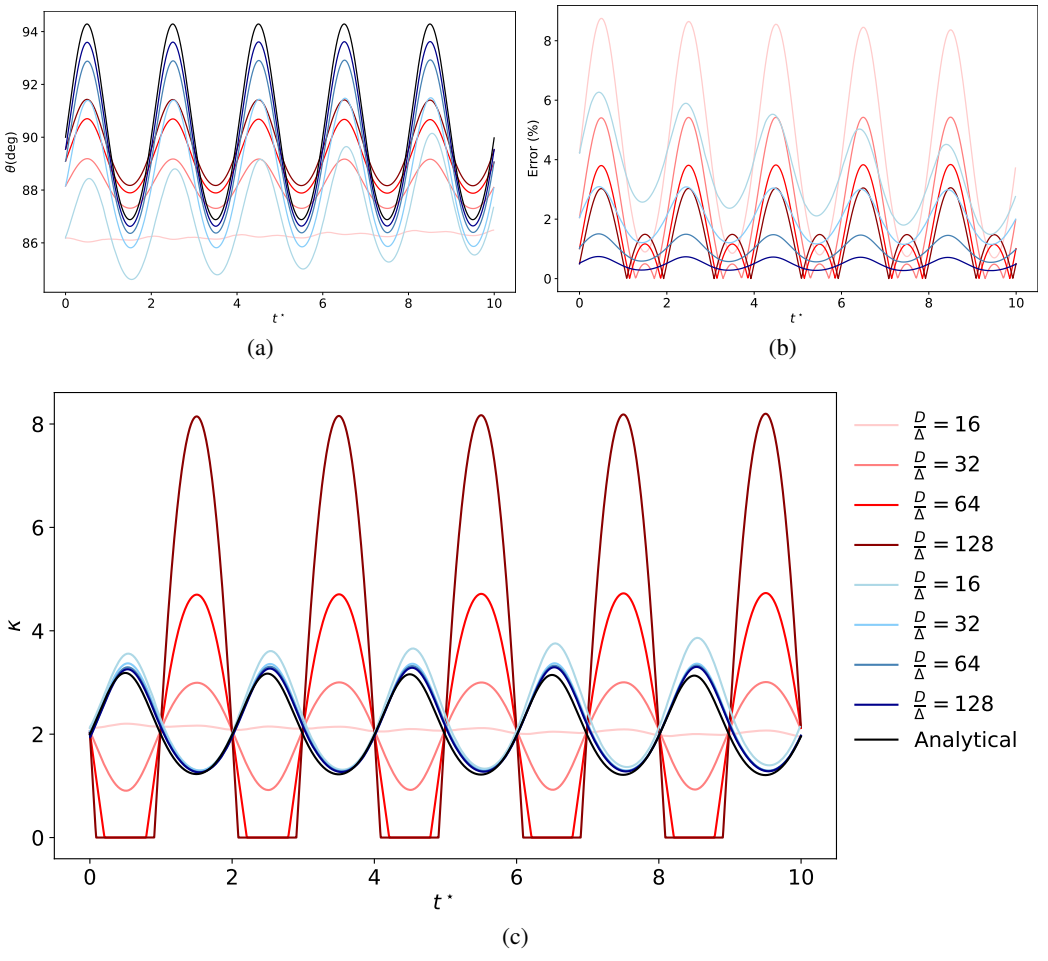

Figure 4: Validation of the angle extrapolation method. The plots depict various aspects against dimensionless time, with the red color denoting the 90° case and blue indicating the imposition of the extrapolation method. The shading from light to dark corresponds to increasing points per diameter. (a) The transport of the contact angle reveals superior convergence with the extrapolation method. (b) The error in the contact angle over time, peaking when disk deformation is maximal. (c) Curvature transport over dimensionless time, illustrating divergence in the 90° case and convergence towards the analytical solution in the other scenario.

of this additional stagnation point depend on the viscosity ratio, although our primary focus is not on this aspect.

4.1. *Grid independency and transition to film entrainment*

In the pulling plate setup, a distinctive characteristic is the presence of a de-wetting transition capillary number $\mathrm{Ca}_{\mathrm{tr}}$, marking the point beyond which liquid film entrainment occurs, leading to an absence of a steady-state position for the contact line. Previous numerical results by Afkhami *et al.* (2018) identified this transition capillary number, but it was grid-dependent. Using the GNBC method, with ε resolved (ie. larger than the grid size Δ), we achieve a grid-independent $\mathrm{Ca}_{\mathrm{tr}}$. Figure 6 illustrates this, plotting the contact line position (representing

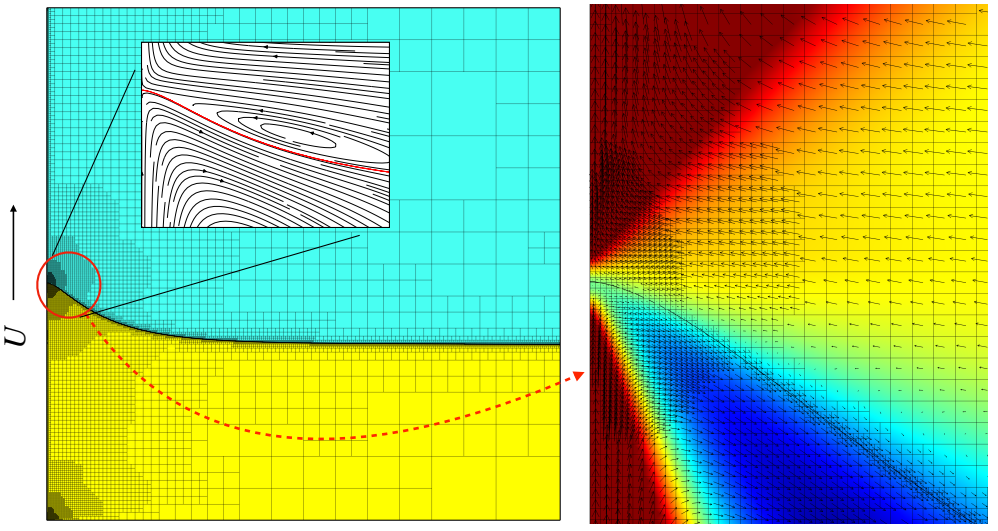

Figure 5: Steady-state meniscus example for Ca = 0.1 using our GNBC method with $\varepsilon = 0.05$. The Figure is in the contact line's reference frame, where the left plate is pulled up with $U_w = \sqrt{\text{Ca}}$. The inset, a zoomed image depicting the flow field, highlights the contact line as a stagnation point. Notably, there is an additional stagnation point in the upper phase, as indicated by the streamlines. Both the GNBC delta function width and the slip length are set to ε.

the fluid film height) over time. For $\text{Ca} \leqslant 0.12$, a steady-state height is eventually reached; however, for Ca = 0.14, the height continually increases. Thus, we determine that Ca_{tr} for this case is $\text{Ca} = 0.13 \pm 0.01$. The influence of Young's stress is evident when comparing Figure 6a with Figure 6b. The Ca_{tr} remains the same, but the steady-state heights exhibit a slight decrease.

We now conduct a convergence study to demonstrate grid independence of the GNBC. In Figure 7a, we present interface shapes for a fixed Ca = 0.12 and $\varepsilon = 0.2$ with varying resolutions, showing apparent convergence. In Figure 8, we display the percentage error in the contact line position for this case, revealing second-order convergence. This confirms that our GNBC method achieves grid independence for steady-state height with a fixed Ca and ε, including the Ca_{tr}. As a comparison, Figure 7b illustrates a similar convergence study for the no-slip case, presenting steady-state interface shapes for a fixed Ca = 0.04 and a constant capillary length l_c with varying grid sizes. Unlike the GNBC case, there is no convergence in the steady-state height. Notably, for a grid resolution of $\frac{l_c}{\Delta} = 200$, the Ca = 0.04 surpasses the transition point Ca_{tr}. This aligns with the findings of Afkhami *et al.* (2018), emphasizing the grid dependence of Ca_{tr} in the no-slip scenario. Thus, our GNBC method has shown a significant improvement by removing this grid dependence.

With our resolved GNBC, the parameters influencing Ca_{tr} are ε and the equilibrium contact angle (θ_{eq}), not the grid size. This aligns with expectations, as these are the only two variables† considered, apart from fluid properties.

Figure 9 illustrates Ca_{tr} as a function of ε and θ_{eq}. A decrease in ε width and θ_{eq} corresponds to a decrease in Ca_{tr}. The dependence on the equilibrium contact angle is notably linear. While this linearity may break at smaller angles, it's important to note that our

† For simplicity, the ratio of the smoothed delta function width to the slip length is assumed to be 1.

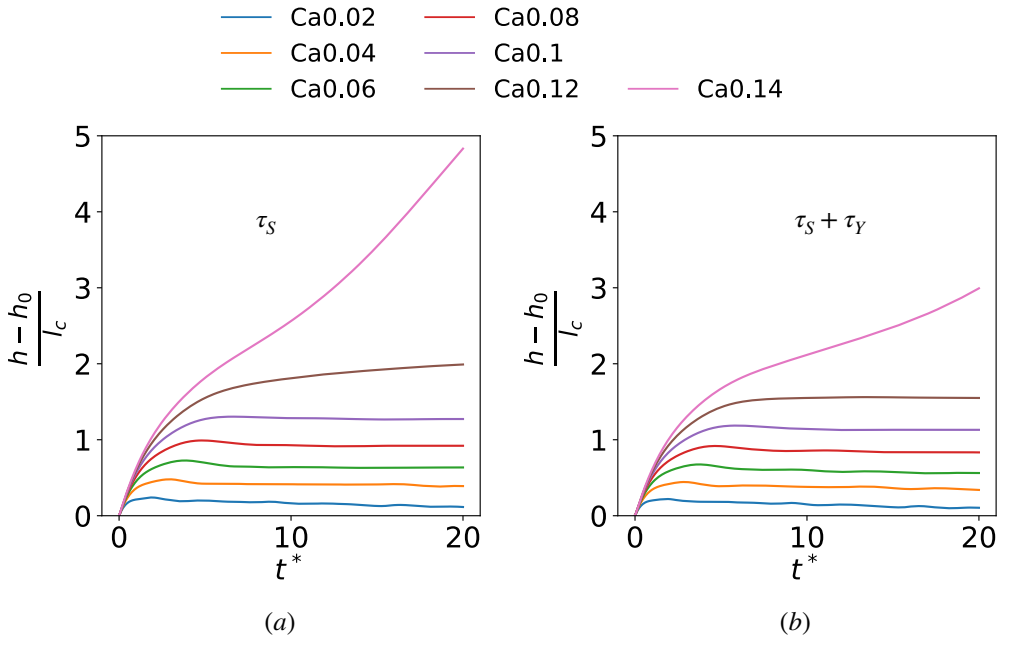

Figure 6: Vertical height of the contact line as a function of time for different capillary numbers Ca, presented separately for (a) shear stress only and (b) both Young stress and shear stress. Steady-state heights are achieved, and a transition $\mathrm{Ca_{tr}}$ is observed, beyond which the liquid film rises continuously. In both (a) and (b), $\mathrm{Ca_{tr}} = 0.13$. Simulations are conducted with $\varepsilon = 0.05$, $\theta_e = 90^\circ$, and a resolution of $\varepsilon/\Delta = 5.12$.

solver, which employs only horizontal heights, faces limitations in handling angles smaller than 30°.

4.2. *Steady-state contact line dynamics: the GNBC smoothing signature*

We demonstrate the full regularization of the contact line singularity achieved by our GNBC method. Figure 10 presents the curvature as a function of the distance from the contact line for various grid resolutions. The Navier slip model exhibits a logarithmic divergence in curvature, consistent with the analytical findings of Devauchelle *et al.* (2007) and Kulkarni *et al.* (2023). While the singularity in the Navier slip model is integrable and considered 'weak,' it induces pressure singularities, rendering the slip model thermodynamically ill-posed. In contrast, our GNBC method regularizes the logarithmically singular curvature at the contact line ($\kappa \sim \log r$), establishing it as a thermodynamically well-posed model.

In their work, Fricke *et al.* (2019) demonstrated that assuming a C^1 velocity field up to the contact line allows the proof that, in the reference frame of the solid wall, the rate of change of the contact angle scales with the shear stress at the contact line. Mathematically, this implies $\dot{\theta}_\mathrm{d} = \frac{\partial u}{2\partial x}$. In steady state, where $\dot{\theta}_\mathrm{d} = 0$, the shear stress, denoted as $\frac{\partial u}{\partial x}$, must approach zero as one approaches the contact line. A non-zero $\frac{\partial u}{\partial x}$ would indicate a violation of the smoothness assumption made by Fricke *et al.* (2019). This violation occurs in the Navier slip model, where $\frac{\partial u}{\partial x} \neq 0$ is necessary for contact line motion. In Figure 11, we observe the behavior of shear stress for both Navier slip and GNBC in steady state. The shear stress at the contact line converges to zero within the ε region for GNBC, aligning with the expected smoothness of the flow field. However, for the Navier slip model, the shear stress fails to converge to zero.

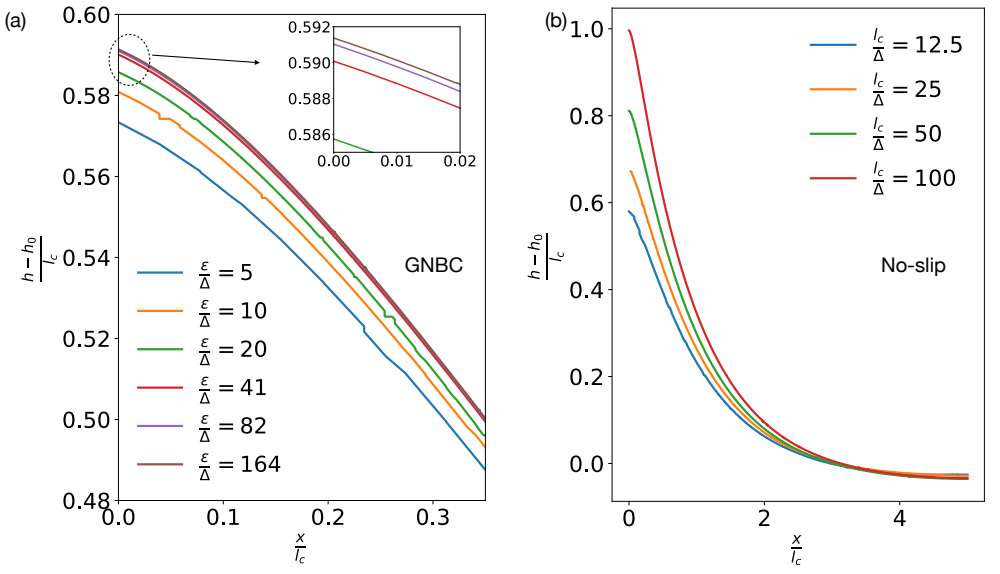

Figure 7: Steady-state height and interface shapes near the contact line with varying grid resolution for (a) GNBC and (b) No-slip. In (a), Ca = 0.12 and $\varepsilon = 0.2$ are fixed, showing convergent interface shapes. In (b), fixed Ca = 0.04 reveals that due to implicit slip, steady-state solutions are achievable even with a no-slip boundary condition. Interface shapes do not converge with grid refinement, and no steady-state height is found at resolutions higher than $\frac{l_c}{\Delta} > 100$. This emphasizes the grid independence in (a) with GNBC, while (b) exhibits clear grid dependence.

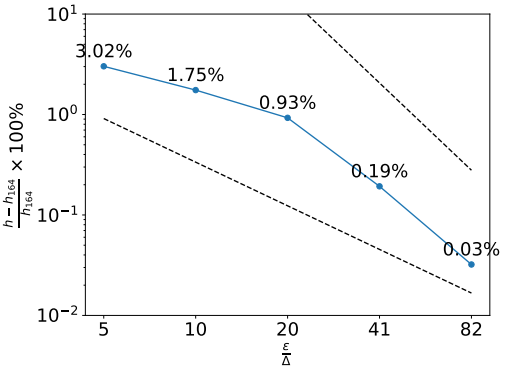

Figure 8: Percentage error in the contact line position for steady-state interface shapes obtained in Figure 7a. The reference solution is taken at 164 grid points per slip length $\frac{\varepsilon}{\Delta}$, and the dashed lines represent second-order and first-order convergence. It is observed that above 20 grid points per ε, a second-order convergence is achieved.

Having demonstrated that the shear stress at the contact line is zero for GNBC in the steady state, we proceed to compare the quasi-stationary state GNBC law (2.18) with our simulation results in Figure 12. Remarkably, we observe an excellent agreement between the simulation outcomes and the quasi-stationary GNBC law, particularly up to $\mathrm{Ca} < \mathrm{Ca}_{\mathrm{tr}}$. It is essential to note that the behavior of $\mathrm{Ca}_{\mathrm{cl}} = f(\theta_{\mathrm{s}})$ in Figure 12, as per the quasi-stationary GNBC law (2.15), is not explicitly imposed but is an outcome derived from our simulations.

Our GNBC smoothing is seen only inside the $r < \varepsilon$ region meaning that the outer region

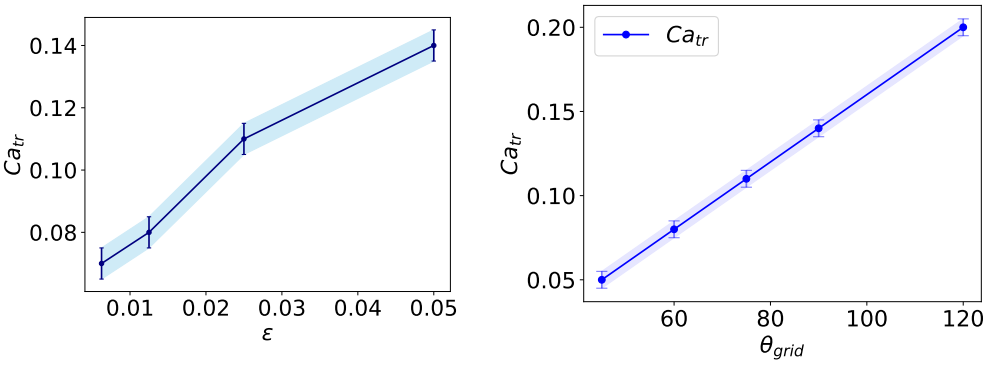

(a) (b)

Figure 9: Transition capillary number plotted against (a) ε and (b) θ_e. All simulations incorporate both Young's stress and shear stress, employing the flow-consistent Generalized Navier Boundary Condition (GNBC). In (a), $\theta_e = 90^\circ$, and in (b), $\varepsilon = 0.05$. The resolution for all simulations is maintained at $\frac{\varepsilon}{\Delta} = 5.12$.

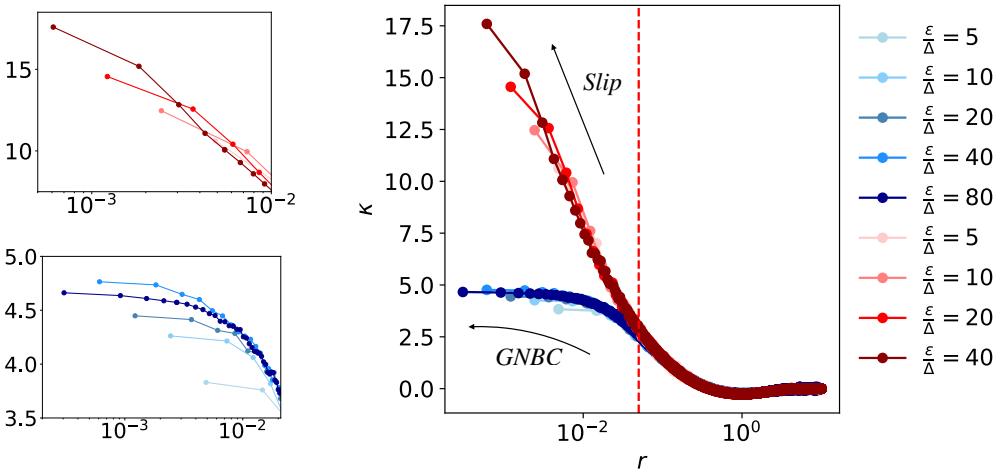

Figure 10: Curvature profiles relative to the radial distance from the contact line. The red curves represent curvature under the Navier slip boundary condition (NBC), exhibiting a logarithmic divergence. In contrast, the blue curves illustrate curvature under the Generalized Navier Boundary Condition (GNBC), demonstrating convergence to a finite value and eliminating the singularity present in the NBC. Simulations are conducted with Ca = 0.08 and $\varepsilon = 0.05$. The equilibrium angle is $\theta_e = 90^\circ$, and Δ denotes the grid size. Various color intensities denote grid refinement, where lighter shades correspond to a coarse mesh, and darker shades indicate a fine mesh.

solution and intermediate asymptotic remain the same and in line with those that are well-known in the literature (Afkhami *et al.* 2018). Cox (1986) did an asymptotic expansion in powers of Ca and showed that for any slip-like model, there exists an intermediate scale where the interface bending behaves as per the following Cox-law

$$G(\theta_d) - G(\theta(r)) = -Ca \log \frac{r}{\varepsilon} + Ca \frac{a_0}{f(\theta_d, \chi)} + O(Ca^2). \tag{4.1}$$

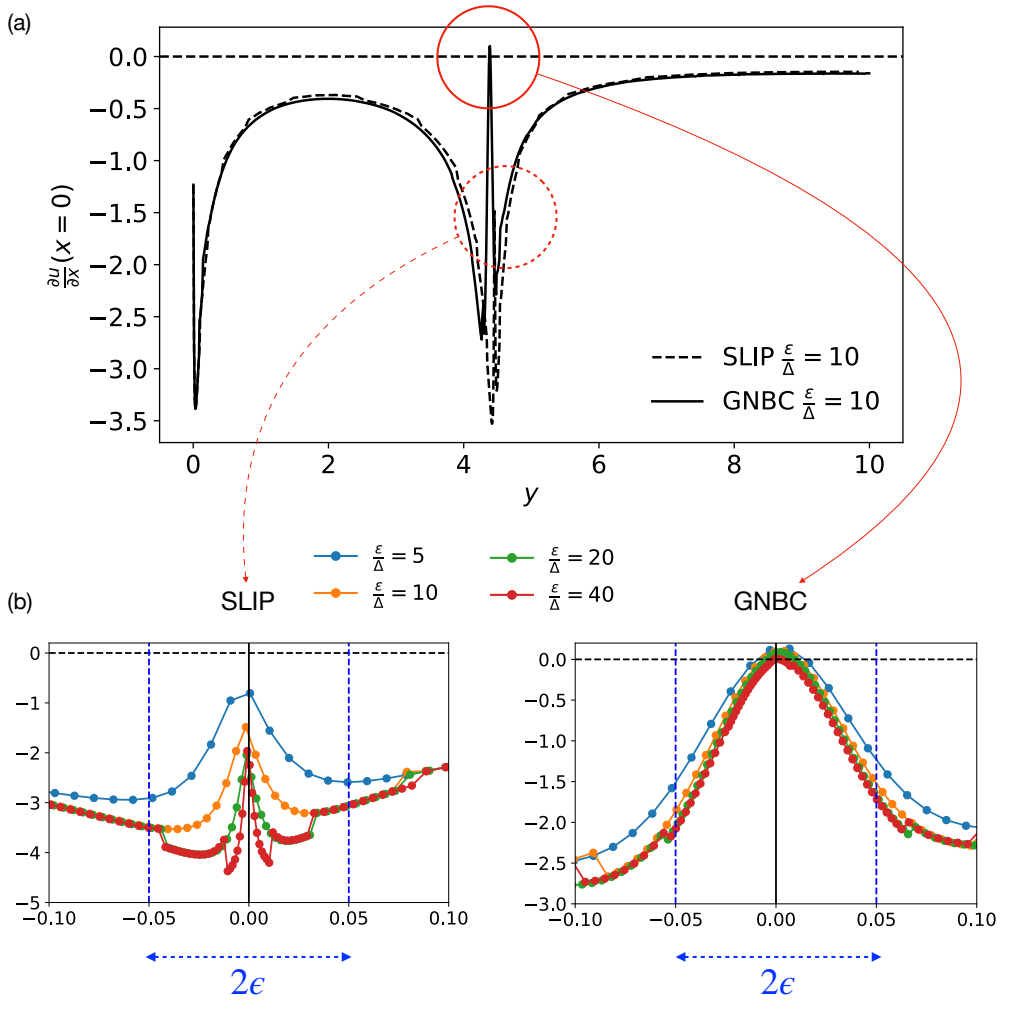

Figure 11: (a) Wall shear stress $\frac{\partial u}{\partial x}$ in a steady-state simulation plotted against the vertical position y. The dashed line corresponds to the Navier slip boundary condition, while the solid line corresponds to the GNBC. Both curves largely overlap, except for a small region shown in the zoom-ins for Navier slip and GNBC in (b) and (c) respectively. The zoomed-in figures are normalized by the contact line position, where 0 on the x-axis corresponds to the contact line position. Notably, for (c) GNBC, shear stress at the contact line is zero, whereas it is not the case for (a) Navier slip. Simulations are conducted for Ca = 0.08 with a fixed $\varepsilon = 0.05$ for varying grid sizes.

In above equation, $G(\theta)$ is the Cox function which can be approximated as $G(\theta) = \frac{\theta^3}{9}$, θ_d is the contact angle and $\theta(r)$ s the local angle measured at a distance r. Other parameters include ε which is the slip length or any other microscopic length scale such that the inner region physics is captured only inside $r < \varepsilon$. χ is the viscosity ratio and a_0 is a constant obtained by matching to the outer solution. Afkhami *et al.* (2018) verified above law and presented a wetting theory derived from the numerics where the Cox law (4.1) was written as

$$G(\theta_d) - G(\theta(r)) = Ca \log(r/\ell_{mic}) + \Phi, \tag{4.2}$$

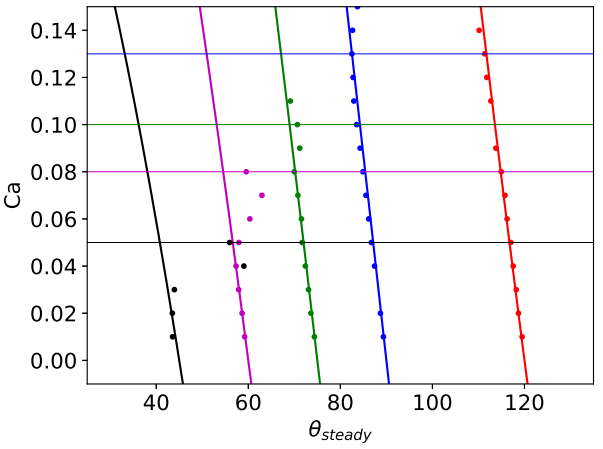

Figure 12: The behavior of the quasi-stationary value of θ_d vs Ca is illustrated for various θ_{eq} and compared with the GNBC law (2.18). The solid lines represent the analytical expression of the steady-state behavior expected from (2.18), while the dots depict simulation results. Horizontal lines denote the $\mathrm{Ca_{tr}}$. Different colors represent various θ_{eq}, progressing from left to right (black to red) as 45°, 60°, 75°, 90°, and 120°, respectively. An excellent agreement between simulations and the GNBC law (2.18) is observed up to $Ca < \mathrm{Ca_{tr}}$.

where ℓ_{mic} is the microscopic length scale which in their paper was the grid size Δ and in current work should be λ. Φ is a gauge function which would be obtained numerically. The reader is referred to the original work of Cox (1986) and the numerical work by Afkhami *et al.* (2018) for the details.

We verify the existence of the region predicted by the (4.2) in figures 13 and 14. These figures also show that the gauge function for the GNBC is always less than the gauge function of the Navier slip. Based on the asymptotic matching section presented in the work by Kulkarni *et al.* (2023), the intermediate region exists where the Cox solution and the inner region solution are of similar order. The Cox law in theory gives us a family of curves in the intermediate region. The final curve is then decided by matching the family to the inner region. In the present case, this means that the matching happens at $r = c\lambda$ where c depends on whether we use the slip boundary condition or the GNBC. A smaller value of Φ implies that the GNBC smoothing influence region is stronger than the slip smoothing inner region. That is $c_{gnbc} > c_{slip}$. This is explicitly shown in Figure 15. We can identify the following two regions, (a) an inner region present at $r \ll c\lambda$ and (b) an intermediate region $r \gg c\lambda$ where we see Cox bending. The matching happens when the two regions are of similar order at $r = c\lambda$. Here c depends on the contact line model used.

4.3. *The transient characteristics of the GNBC numerics*

In the previous section, we demonstrated the steady-state smoothness achieved by GNBC. Starting from a horizontal two-fluid interface at rest, we now compare the transient characteristics of GNBC. A distinctive feature of our GNBC is that the contact angle is not fixed a priori. Figure 16a illustrates the contact angle θ_d as a function of time. It initiates from an initial value of 90° and subsequently relaxes to a steady-state value different from 90°. Although it eventually converges to a steady state, we observe some spurious oscillations in the value of θ_d. These oscillations increase with higher Ca, but their impact is limited as their amplitude remains less than 0.5° and decreases with grid refinement.

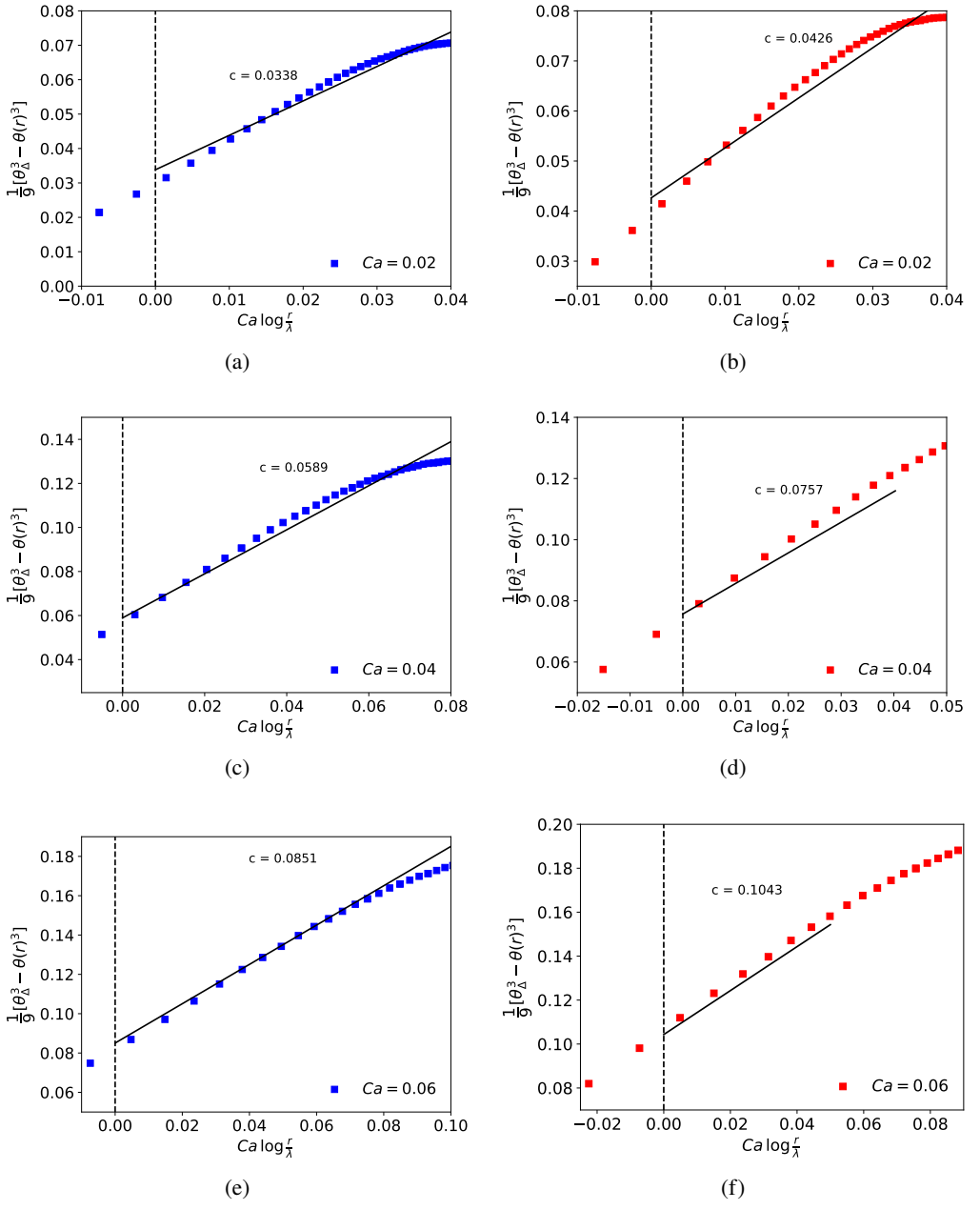

Figure 13: Comparison of the Cox law observed at an intermediate scale in our simulations for GNBC (blue) and Navier slip (red). The vertical dashed line represents the slip length λ, which is equivalent to the GNBC width ε. The solid black lines follow the Cox law (4.2), approximated as $\theta^3\Delta - \theta^3(r) = 9Ca \log \frac{r}{\lambda} + c$. Here, $\theta\Delta$ is the contact angle observed in the simulations at the contact line cell. The value of c is provided in the plot for each case, with a smaller c observed for GNBC. $\theta_{eq} = 90^\circ$ for all simulations, resulting in a constant $\theta_\Delta = 90^\circ$ for Navier slip and $\theta_\Delta = \theta_d$ for GNBC. $\lambda = 0.05$, and the resolution is $\frac{\varepsilon}{\Delta} = 10$ in all cases.

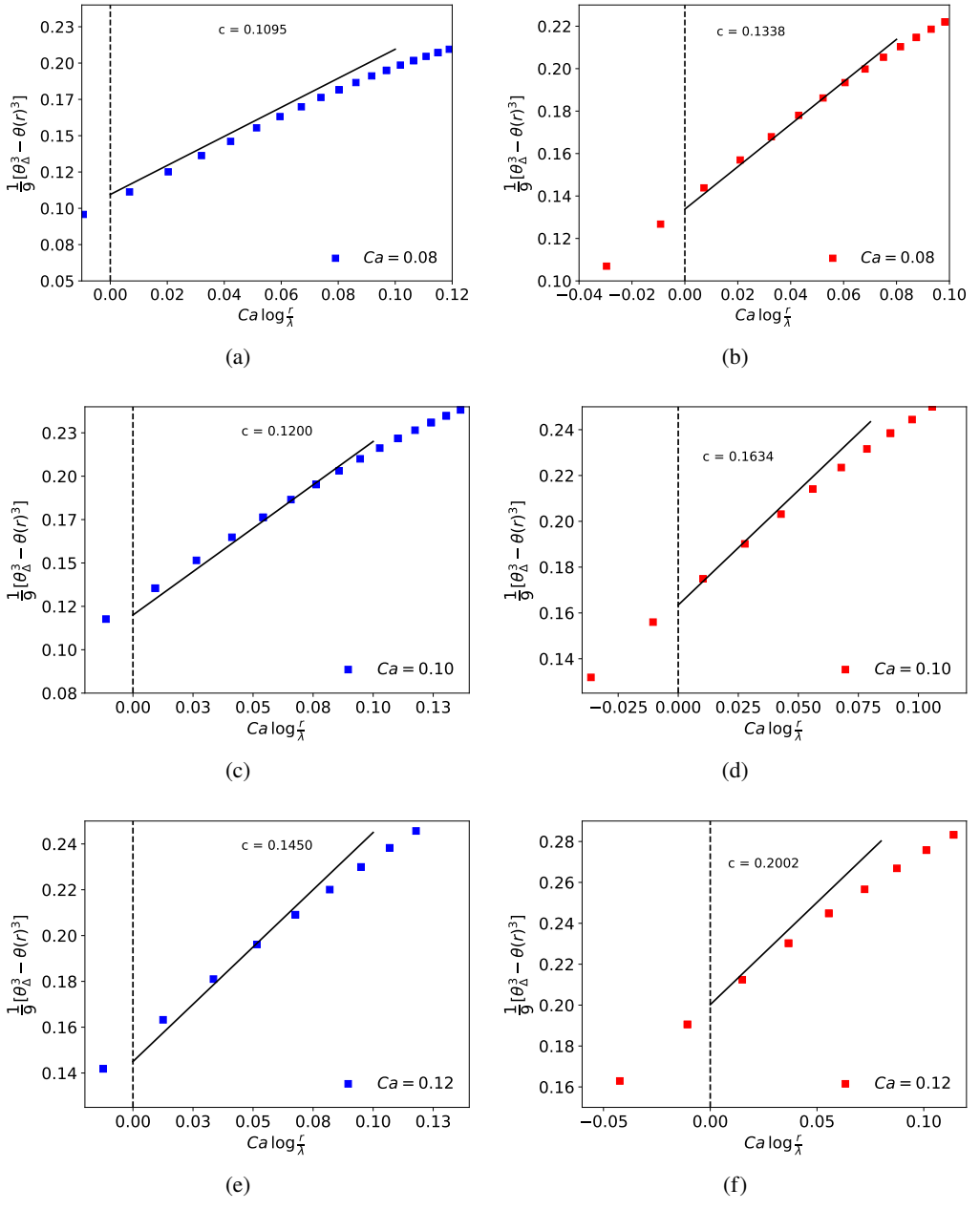

Figure 14: An extension of Figure 13 for higher values of Ca. All parameters remain the same as in Figure 13, except for the Ca values. The matching with the Cox law starts to deteriorate as Ca is increased, aligning with theoretical expectations.

In Figure16a, we observe an interesting trend when plotting θ_d against $\mathrm{Ca}_{\mathrm{loc}}$, depicted in Figure 16b. Here, $\mathrm{Ca}_{\mathrm{loc}}$ signifies the contact line Ca in the lab frame. It starts from 0 as everything is initially at rest and eventually converges back to 0 in a quasi-stationary state. The transient behavior reveals that although we instantaneously set the solid velocity to U_w, $\mathrm{Ca}_{\mathrm{loc}}$ takes some time to reach its maximum velocity. The time required for this is given

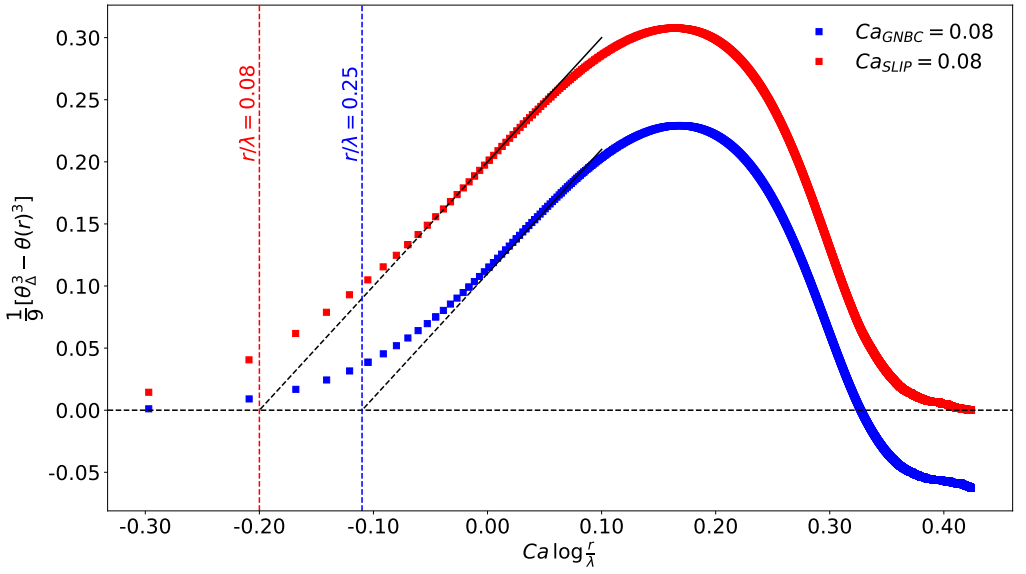

Figure 15: The Cox law matching to the inner region for GNBC and Navier slip. The Cox solution becomes comparable to the inner region at a certain scale $r = c\lambda$. The value of c is 0.08 for Navier slip but is 0.25 for GNBC. The higher value of c indicates a stronger influence from the inner region. Simulations are conducted for $Ca = 0.08$ and $\varepsilon = \lambda = 0.05$. The resolution is $r/\Delta = 20$ for both the slip and GNBC.

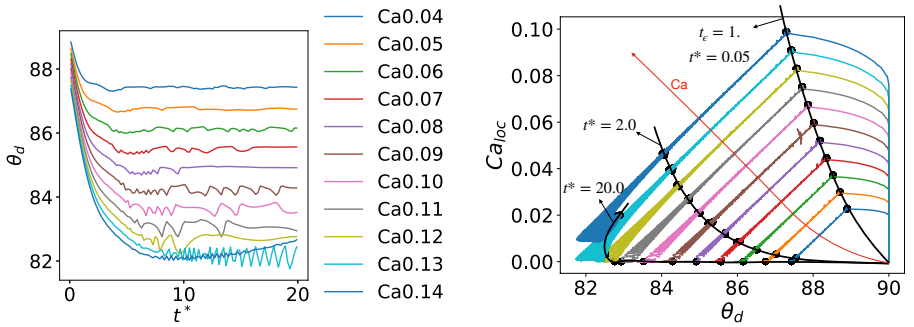

(a) (b)

Figure 16: (a) Evolution of the grid-scale dynamic contact angle θ_d in the GNBC simulation for various Ca. The angle begins to deviate from the initial value of 90° and eventually reaches a steady state. Around $\mathrm{Ca_{tr}}$, the angle exhibits oscillations over time. (b) The relaxation plot on a $\theta - Ca$ plane. Here, $\mathrm{Ca_{loc}}$ represents the contact line capillary number. Time progresses from right to left, and a maximum in $\mathrm{Ca_{loc}}$ is reached at $t_\varepsilon = 1$, which corresponds to the slip length timescale (ε/U_w). After this point, $\mathrm{Ca_{loc}}$ starts relaxing towards a steady state ($\mathrm{Ca_{loc}} = 0$). Beyond $\mathrm{Ca_{tr}}$, $\mathrm{Ca_{loc}}$ reaches a minimum and begins rising again. Simulations are the same as in Figure 6.

by the ε time, denoted as $t_\varepsilon = \varepsilon/U_w$. This implies that t_ε acts as a relaxation timescale stemming from contact line friction. A detailed examination of behavior for $t < t_\varepsilon$ is beyond the current study's scope. Once $\mathrm{Ca_{loc}}$ reaches its maximum, it starts relaxing to the steady state where $\mathrm{Ca_{loc}} = 0$, and θ_d adheres to the GNBC law shown in Figure 12.

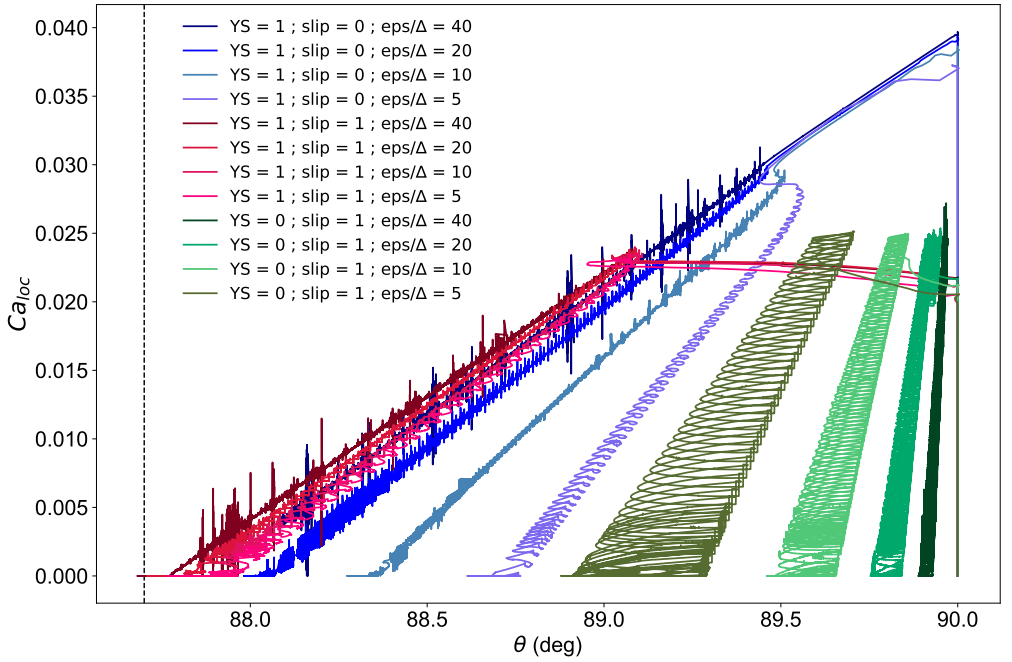

Figure 17: The relaxation plot on the $\mathrm{Ca_{loc}}$-θ plane for GNBC (YS=1; slip=1), NBC (YS=0; slip=1), and no-slip with Young stress (YS=1; slip=0). All the plots are done for Ca = 0.04 and $\varepsilon = 0.05$. The grid resolution is reported in terms of ε/Δ, and color intensity is increased to show higher resolution. The dashed black line represents the GNBC law angle in the steady state. Time flows from right to left and aligns the curves. Each curve set has its own characteristic feature. The blue (YS=1; slip=0) case rises suddenly to Ca as expected and then relaxes to the steady-state value. In the steady state, it converges to the GNBC law θ_d. We also observe that the steady-state value converges with grid refinement, and the spurious oscillations in the angle are reduced with grid refinement. The green case (YS=0; slip=1) rises to max $\mathrm{Ca_{loc}}$ < Ca in the relaxation time t_ε, then it converges to the constant value of 90° contact angle as the grid is refined. The red case, GNBC (YS=1; slip=1), has characteristics of both of the former cases, that is, rises to the max $\mathrm{Ca_{loc}}$ < Ca in t_ε and then relaxes to the GNBC law angle. Note that GNBC (YS=1; slip=1) outperforms both the other cases even with a small refinement of $\varepsilon/\Delta = 5$, showing fewer spurious oscillations than NBC (YS=0; slip=1) and higher accuracy in converging to the GNBC law angle than the only Young stress curve (YS=1; slip=0).

In Figure 17, we illustrate the behavior of each term of the GNBC equation 3.7. We analyze and present each outcome for three different boundary conditions:

(i) Navier slip with a constant contact angle $\theta_d = \theta_e$, denoted (YS = 0; slip = 1)

$$\mathbf{v}_\parallel + \frac{1}{\beta}(\mathbf{S}\mathbf{n}_{\partial\Omega})_\parallel = \mathbf{U}_w \quad \text{on} \quad \partial\Omega, \tag{4.3}$$

(ii) No slip with uncompensated Young stress, with the "free angle" method (3.8), denoted (YS = 1; slip = 0)

$$\mathbf{v}_\parallel = \mathbf{U}_w + \frac{1}{\beta}\,\mathrm{f}(\frac{x}{\varepsilon})\,\sigma(\cos\theta_\mathrm{e} - \cos\theta_\mathrm{d})\,\mathbf{n}_\Gamma \quad \text{on} \quad \partial\Omega, \tag{4.4}$$

(iii) Full GNBC as written in Equation (3.7) that combines contributions from both the above cases, denoted (YS = 1; slip = 1).

We conduct simulations for each individual case (i), (ii), and (iii), and illustrate the behavior of each term on a $\mathrm{Ca}_{\mathrm{loc}} - \theta$ plane in Figure 17. The timeline in this figure progresses from right to left. For case (i) Navier slip (depicted by green curves), we observe that at $t = 0$ and $\theta_d = 90^{\circ}$, when the interface is horizontal, $\mathrm{Ca}_{\mathrm{loc}}$ is null. Then, $\mathrm{Ca}_{\mathrm{loc}}$ suddenly rises to a maximum value, which remains lower than the imposed Ca. This rapid rise occurs within the relaxation time t_ε, where ε is the slip length. This behavior aligns with the discussion in Figure 16b. Subsequently, the contact line relaxes to a steady state where $\mathrm{Ca}_{\mathrm{loc}}$ returns to zero. This relaxation is accompanied by spurious oscillations in the contact angle θ_d. Ideally, in this case, the system should relax to $\theta_d = 90^{\circ}$ throughout the motion and also in the steady state (given that we impose a constant $\theta_d = \theta_e = 90^{\circ}$), which is indeed observed as the grid is refined. The final angle θ_d converges to 90°, and spurious oscillations diminish with increasing grid refinement.

In case (ii) No slip with Young's stress (shown in blue curves), we notice an interesting pattern. At the start (t=0), the simulation begins with $\mathrm{Ca}_{\mathrm{loc}} = 0$ and $\theta_d = 90^{\circ}$ at the lower right of Figure 17. However, as soon as we advance in time, $\mathrm{Ca}_{\mathrm{loc}}$ increases to a maximum value equal to Ca, subsequently, starts relaxing to 0. With the presence of uncompensated Young stress, it ideally should relax to the GNBC law angle indicated by the dashed line in Figure 17. We observe that oscillations are decreasing with grid refinement and the final angle value is converging towards the GNBC law angle.

In the case of (iii) with Full GNBC (depicted by red curves), we observe characteristics from both (i) and (ii). Initially, both $\mathrm{Ca}_{\mathrm{loc}}$ and θ_{d} start from zero. Subsequently, $\mathrm{Ca}_{\mathrm{loc}}$ reaches a maximum during the relaxation time and eventually relaxes to the GNBC law angle. The notable advantage of the full GNBC is that even with a modest resolution of 5 grid points per slip length, the spurious oscillations, compared to case (i) at the same resolution, are significantly reduced. Moreover, the accuracy in relaxing towards the GNBC law angle (dashed line) is substantially improved compared to case (ii). Further grid refinement leads to a continued reduction in spurious oscillations and enhances accuracy in relaxing towards the GNBC law.

5. Conclusion and Outlook

To summarize, we have developed an implementation of the Generalized Navier Boundary Condition in a geometrical Volume-of-Fluid method. In this method, the dynamic contact angle is not prescribed geometrically but is controlled by kinematics through the velocity boundary condition. This is achieved by reconstructing the contact angle at the boundary using the interface normal and the curvature one cell layer away from the boundary. We validate the resulting "free angle methodology" by studying the interface advection problem in the presence of a moving contact line in Section 3.2. In the present approach, the uncompensated Young stress is distributed over a characteristic width ε which is defined independently of the mesh size. Using the kinematic evolution equation of the dynamic contact angle (1.4), we show rigorously that the solution obeys the "GNBC law" (2.17), if the solution has a C^1-regularity up to the contact line. Indeed, we show in Section 4 that the weak singularity at the contact line is removed in the GNBC model with finite ε. We find a mesh-converging curvature at the contact line (see Fig. 10) and the numerical solution satisfies the GNBC law in a quasi-stationary state (i.e. for $\dot{\theta}_{\mathrm{d}} = 0$). These results are consistent with the recent findings of Kulkarni *et al.* (2023) who showed that this model indeed shows a local C^2-regularity at the contact line. As expected from kinematics, the tangential stress

component goes to zero at the contact line in quasi-stationary states (see Fig. 11). In this sense, we observe perfect apparent slip at the moving contact line.

5.1. *Outlook: A non-linear generalization of the GNBC*

As discussed in detail in Section 2.2, the GNBC in the form

$$-\beta(\mathbf{v}_\parallel - \mathbf{U}_w) = (\mathbf{S}\mathbf{n}_{\partial\Omega})_\parallel + \sigma(\cos\theta_\mathrm{d} - \cos\theta_\mathrm{e})\,\mathbf{n}_\Gamma\delta_\Gamma \quad \text{on} \quad \partial\Omega \tag{5.1}$$

is obtained as a *linear* closure relation, to render the dissipation integral

$$\mathcal{T} = \int_{\partial\Omega} \left((\mathbf{S}\mathbf{n}_{\partial\Omega})_\parallel + \sigma(\cos\theta_\mathrm{d} - \cos\theta_\mathrm{e})\,\mathbf{n}_\Gamma\delta_\Gamma\right)\cdot(\mathbf{v}_\parallel - \mathbf{U}_w)\,dA. \tag{5.2}$$

non-positiv. Since, according to kinematics, the viscous stress contribution vanishes in a quasi-stationary state, we obtain the dynamic contact angle relation

$$-\zeta U_\mathrm{cl} = \sigma(\cos\theta_\mathrm{d} - \cos\theta_\mathrm{e}) \tag{5.3}$$

with the contact line friction coefficient $\zeta = \beta\varepsilon$. Notably, equation (5.3) is also found in the Molecular Kinetic Theory (MKT) in the limit of low capillary number (see, e.g., Blake *et al.* (2015)). However, for higher capillary numbers, the MKT predicts that†

$$U_\mathrm{cl} = 2\kappa^0\lambda\sinh\left[\sigma\,(\cos\theta_\mathrm{e} - \cos\theta_\mathrm{d})\,/(2nk_BT)\right]. \tag{5.4}$$

Therefore, it is interesting to think about a possible closure relation for (5.2) that will lead to the relation (5.4) in quasi-stationary states. Notice that (5.4) can be linearized for $U_\mathrm{cl} \to 0$ using $\sinh(x) = x + O(x^3)$. Hence, the contact line friction coefficient is identified as $\zeta = (nk_BT)/(\kappa^0\lambda)$.

For simplicity, let us assume that $\mathbf{U}_w = 0$ in the following (the generalization to $\mathbf{U}_w \neq 0$ is obvious). To proceed, it is useful to decompose the integral in (5.2) into its components normal and tangential to the contact line, using the decomposition

$$\mathbf{v}_\parallel = \mathbf{n}_\Gamma(\mathbf{v}_\parallel\cdot\mathbf{n}_\Gamma) + \mathbf{t}_\Gamma(\mathbf{v}_\parallel\cdot\mathbf{t}_\Gamma).$$

Here, we denote by $\mathbf{t}_\Gamma$ the tangent vector to the contact line. We obtain the representation

$$\mathcal{T} = \mathcal{T}_\perp + \mathcal{T}_\parallel \tag{5.5}$$

with

$$\mathcal{T}_\parallel = \int_{\partial\Omega} \left(\mathbf{t}_\Gamma\cdot(\mathbf{S}\mathbf{n}_{\partial\Omega})_\parallel\right)(\mathbf{t}_\Gamma\cdot\mathbf{v}_\parallel)\,dA$$

and

$$\mathcal{T}_\perp = \int_{\partial\Omega} \left(\mathbf{n}_\Gamma\cdot(\mathbf{S}\mathbf{n}_{\partial\Omega})_\parallel + \sigma(\cos\theta_\mathrm{d} - \cos\theta_\mathrm{e})\,\delta_\Gamma\right)(\mathbf{n}_\Gamma\cdot\mathbf{v}_\parallel)\,dA. \tag{5.6}$$

We are now looking for closure relations to ensure that $\mathcal{T}_\perp \leqslant 0$ and $\mathcal{T}_\parallel \leqslant 0$. Motivated by (5.4), we may choose

$$\boxed{\mathbf{v}_\parallel\cdot\mathbf{n}_\Gamma = a\sinh\left(\frac{-\mathbf{n}_\Gamma\cdot(\mathbf{S}\mathbf{n}_{\partial\Omega})_\parallel + \sigma(\cos\theta_\mathrm{e} - \cos\theta_\mathrm{d})\,\delta_\Gamma}{b}\right)} \tag{5.7}$$

† In this case, the average distance and equilibrium frequency of molecular jumps are denoted by λ and κ^0, respectively. Moreover, n is the number of adsorption sites per unit area, k_B is the Boltzmann constant and T is the absolute temperature; see Blake *et al.* (2015) for more details.

with positive constants $a = 2\kappa^0\lambda$ and $b = 2nk_BT$. This closure is consistent with the entropy principle because

$$ax \sinh(-x/b) \leqslant 0 \quad \text{for all } x \in \mathbb{R}$$

if $a, b > 0$. Clearly, Equation (5.7) reduces to the original GNBC (5.1) with $\beta = b/a$ if $\mathbf{v}_{\|} \cdot \mathbf{n}_\Gamma \to 0$. Since it corresponds to the MKT (5.4) for quasi-stationary states, it may improve the standard GNBC model for higher values of the capillary number. This shall be studied in detail in the future.

Acknowledgements.

Funding. This project has received funding from the European Research Council (ERC) under the European Union's Horizon 2020 research and innovation programme (grant agreement n° 883849). MF and DB acknowledge the financial support by the German Research Foundation (DFG) within the Collaborative Research Centre 1194 (Project-ID 265191195).

REFERENCES

Afkhami, S., Buongiorno, J., Guion, A., Popinet, S., Saade, Y., Scardovelli, R. & Zaleski, S. 2018 Transition in a numerical model of contact line dynamics and forced dewetting. *Journal of Computational Physics* **374**, 1061–1093.

Afkhami, S. & Bussmann, M. 2008 Height functions for applying contact angles to 2D VOF simulations. *International Journal for Numerical Methods in Fluids* **57** (4), 453–472.

Afkhami, S. & Bussmann, M. 2009 Height functions for applying contact angles to 3D VOF simulations. *International Journal for Numerical Methods in Fluids* **61** (8), 827–847.

Blake, T.D & Haynes, J.M. 1969 Kinetics of liquid-liquid displacement. *Journal of Colloid and Interface Science* **30** (3), 421–423.

Blake, T. D. 2006 The physics of moving wetting lines. *Journal of Colloid and Interface Science* **299** (1), 1–13.

Blake, Terence D., Clarke, Andrew & Ruschak, Kenneth J. 1994 Hydrodynamic assist of dynamic wetting. *AIChE Journal* **40** (2), 229–242.

Blake, T. D., Fernandez-Toledano, J.-C., Doyen, G. & De Coninck, J. 2015 Forced wetting and hydrodynamic assist. *Physics of Fluids* **27** (11), 112101.

Bonn, D., Eggers, J., Indekeu, J., Meunier, J. & Rolley, E. 2009 Wetting and spreading. *Reviews of Modern Physics* **81** (2), 739–805.

Chen, Xianyang, Lu, Jiacai & Tryggvason, Grétar 2019 Numerical simulation of self-propelled non-equal sized droplets. *Physics of Fluids* **31** (5), 052107.

Cox, R. G. 1986 The dynamics of the spreading of liquids on a solid surface. part 1. viscous flow. *Journal of Fluid Mechanics* **168**, 169–194.

Devauchelle, O., Josserand, C. & Zaleski, S. 2007 Forced dewetting on porous media. *Journal of Fluid Mechanics* **574**, 343–364.

Duffy, Brian R. & Wilson, Stephen K. 1997 A third-order differential equation arising in thin-film flows and relevant to tanner's law. *Applied Mathematics Letters* **10**, 63–68.

Eggers, Jens 2004 Hydrodynamic theory of forced dewetting. *Phys. Rev. Lett.* **93**, 094502.

Fricke, M. 2021 Mathematical modeling and volume-of-fluid based simulation of dynamic wetting. PhD thesis, TU Darmstadt.

Fricke, M. & Bothe, D. 2020 Boundary conditions for dynamic wetting - A mathematical analysis. *The European Physical Journal Special Topics* **229** (10), 1849–1865.

Fricke, M., Köhne, M. & Bothe, D. 2019 A kinematic evolution equation for the dynamic contact angle and some consequences. *Physica D: Nonlinear Phenomena* **394**, 26–43.

Fricke, M., Köhne, M. & Bothe, D. 2018 On the kinematics of contact line motion. *PAMM* **18** (1), e201800451.

Fricke, M., Marić, T. & Bothe, D. 2020 Contact Line Advection using the geometrical Volume of Fluid Method. *Journal of Computational Physics* **407**, 109221.

Fullana, T., Zaleski, S. & Popinet, S. 2020 Dynamic wetting failure in curtain coating by the Volume-of-Fluid method. *The European Physical Journal Special Topics* **229** (10), 1923–1934.

de Gennes, P.-G., Brochard-Wyart, F. & Quéré, D. 2004 *Capillarity and Wetting Phenomena*. New York, NY: Springer New York.

Gerbeau, J.-F. & Lelièvre, T. 2009 Generalized Navier boundary condition and geometric conservation law for surface tension. *Computer Methods in Applied Mechanics and Engineering* **198** (5-8), 644–656.

Hocking, L. M. 2001 Meniscus draw-up and draining. *European Journal of Applied Mathematics* **12** (3), 195–208.

Huh, C. & Mason, S. G. 1977 The steady movement of a liquid meniscus in a capillary tube. *Journal of Fluid Mechanics* **81** (03), 401–419.

Huh, C. & Scriven, L. E 1971 Hydrodynamic model of steady movement of a solid/liquid/fluid contact line. *Journal of Colloid and Interface Science* **35** (1), 85–101.

Jacqmin, David 2000 Contact-line dynamics of a diffuse fluid interface. *Journal of Fluid Mechanics* **402**, 57–88.

Kawakami, K., Kita, Y. & Yamamoto, Y. 2023 Front-tracking simulation of the wetting behavior of an impinging droplet using a relaxed impermeability condition and a generalized navier boundary condition. *Computers & Fluids* **251**, 105739.

Kulkarni, Yash, Fullana, Tomas & Zaleski, Stephane 2023 Stream function solutions for some contact line boundary conditions: Navier slip, super slip and the generalized navier boundary condition. *Proceedings of the Royal Society A: Mathematical, Physical and Engineering Sciences* **479** (2278).

Lukyanov, A. V. & Pryer, T. 2017 Hydrodynamics of moving contact lines: Macroscopic versus microscopic. *Langmuir* **33** (34), 8582–8590.

Lācis, U., Johansson, P., Fullana, T., Hess, B., Amberg, G., Bagheri, S. & Zaleski, S. 2020 Steady moving contact line of water over a no-slip substrate. *The European Physical Journal Special Topics* **229** (10), 1897–1921.

Marengo, Marco & De Coninck, Joel, ed. 2022 *The Surface Wettability Effect on Phase Change*. Springer International Publishing.

Marić, T., Kothe, D. B. & Bothe, D. 2020 Unstructured un-split geometrical Volume-of-Fluid methods – A review. *Journal of Computational Physics* **420**, 109695.

Popinet, S. 2009 An accurate adaptive solver for surface-tension-driven interfacial flows. *Journal of Computational Physics* **228** (16), 5838–5866.

Popinet, S. 2015 A quadtree-adaptive multigrid solver for the serre–green–naghdi equations. *J. Comput. Phys.* **302**, 336–358.

Popinet, S. 2018 Numerical Models of Surface Tension. *Annual Review of Fluid Mechanics* **50** (1), 49–75.

Popinet, Stéphane & Zaleski, Stéphane 1999 A front-tracking algorithm for accurate representation of surface tension. *International Journal for Numerical Methods in Fluids* **30** (6), 775–793.

Prüss, J. & Simonett, G. 2016 *Moving interfaces and quasilinear parabolic evolution equations*. *Monographs in Mathematics* . Switzerland: Birkhäuser.

Qian, T., Wang, X.-P. & Sheng, P. 2003 Molecular scale contact line hydrodynamics of immiscible flows. *Physical Review E* **68** (1 Pt 2), 016306.

Qian, T., Wang, X.-P. & Sheng, P. 2006*a* A variational approach to moving contact line hydrodynamics. *Journal of Fluid Mechanics* **564**, 333.

Qian, T., Wang, X.-P. & Sheng, P. 2006*b* Molecular hydrodynamics of the moving contact line in two-phase immiscible flows. *Commun. Comput. Phys.* **1** (1), 1–52.

Scardovelli, R. & Zaleski, S. 1999 Direct Numerical Simulation of Free-Surface and Interfacial Flow. *Annual Review of Fluid Mechanics* **31** (1), 567–603.

Shang, Xinglong, Luo, Zhengyuan, Gatapova, Elizaveta Ya., Kabov, Oleg A. & Bai, Bofeng 2018 GNBC-based front-tracking method for the three-dimensional simulation of droplet motion on a solid surface. *Computers & Fluids* **172**, 181–195.

Shikhmurzaev, Y. D. 1993 The moving contact line on a smooth solid surface. *International Journal of Multiphase Flow* **19** (4), 589–610.

Shikhmurzaev, Y. D. 2006 Singularities at the moving contact line. Mathematical, physical and computational aspects. *Physica D: Nonlinear Phenomena* **217** (2), 121–133.

Shikhmurzaev, Y. D. 2008 *Capillary flows with forming interfaces*. Boca Raton: Chapman & Hall/CRC.

Slattery, J. C. 1999 *Advanced transport phenomena. Cambridge Series in Chemical Engineering* . Cambridge: Cambridge University Press.

Snoeijer, J. H. & Andreotti, B. 2013 Moving contact lines: Scales, Regimes, and Dynamical Transitions. *Annual Review of Fluid Mechanics* **45** (1), 269–292.

Thompson, Peter A. & Robbins, Mark O. 1989 Simulations of contact-line motion: Slip and the dynamic contact angle. *Physical Review Letters* **63** (7), 766–769.

Tryggvason, G., Scardovelli, R. & Zaleski, S. 2011 *Direct numerical simulations of gas-liquid multiphase flows*. Cambridge University Press.

Yamamoto, Y., Higashida, S., Tanaka, H., Wakimoto, T., Ito, T. & Katoh, K. 2016 Numerical analysis of contact line dynamics passing over a single wettable defect on a wall. *Physics of Fluids* **28** (8).

Yamamoto, Y., Ito, T., Wakimoto, T. & Katoh, K. 2013 Numerical simulations of spontaneous capillary rises with very low capillary numbers using a front-tracking method combined with generalized navier boundary condition. *International Journal of Multiphase Flow* **51**, 22–32.

Yamamoto, Y., Tokieda, K., Wakimoto, T., Ito, T. & Katoh, K. 2014 Modeling of the dynamic wetting behavior in a capillary tube considering the macroscopic–microscopic contact angle relation and generalized navier boundary condition. *International Journal of Multiphase Flow* **59**, 106–112.

Young, T. 1805 An essay on the cohesion of fluids. *Philosophical Transactions of the Royal Society of London* **95**, 65–87.